

Recoiling Supermassive Black Holes in Spin-flip Radio Galaxies

F.K. Liu¹, Dong Wang¹, and Xian Chen²

ABSTRACT

Numerical relativity simulations predict that coalescence of supermassive black hole (SMBH) binaries not only leads to a spin flip but also to a recoil of the merger remnant SMBHs. In the literature, X-shaped radio sources are popularly suggested to be candidates for SMBH mergers with spin flip of jet-ejecting SMBHs. Here we investigate the spectral and spatial observational signatures of the recoiling SMBHs in radio sources undergoing black hole spin flip. Our results show that SMBHs in most spin-flip radio sources have mass ratio $q \gtrsim 0.3$ with a minimum possible value $q_{\min} \simeq 0.05$. For major mergers, the remnant SMBHs can get a kick velocity as high as 2100 km s^{-1} in the direction within an angle $\lesssim 40^\circ$ relative to the spin axes of remnant SMBHs, implying that recoiling quasars are biased to be with high Doppler-shifted broad emission lines while recoiling radio galaxies are biased to large apparent spatial off-center displacements. We also calculate the distribution functions of line-of-sight velocity and apparent spatial off-center for spin-flip radio sources with different apparent jet reorientation angles. Our results show that the larger the apparent jet reorientation angle is, the larger the Doppler-shifting recoiling velocity and apparent spatial off-center displacement will be. We investigate the effects of recoiling velocity on the dust torus in spin-flip radio sources and suggest that recoiling of SMBHs would lead to “dust poor” AGNs. Finally, we collect a sample of 19 X-shaped radio objects and for each object give the probability of detecting the predicted signatures of recoiling SMBH.

Subject headings: black hole physics — galaxies: active — galaxies: evolution — galaxies: jets — gravitational waves — quasars: general

1. Introduction

In the hierarchical galaxy formation model of the Λ CDM cosmology, massive galaxies are produced by successive galaxy mergers (Kauffmann & Haehnelt 2000; Springel et al.

¹Department of Astronomy, Peking University, 100871 Beijing, China; fkliu@pku.edu.cn

²Kavli Institute for Astronomy and Astrophysics, Peking University, 100871 Beijing, China.

2005). During the merging of galaxies, the supermassive black holes (SMBHs) at centers quickly form hard supermassive black hole binaries (SMBHBs) at a separation of pc -scale, and then may stall for a timescale longer than Hubble time, if the gravitational potential at galactic nucleus is spherical and stellar relaxation is dominated by two-body scattering (Begelman, et al. 1980; Yu 2002). However, the hardening rate of SMBHBs can be boosted and SMBHBs become merged within Hubble time because of triaxial or rotating structures, massive perturbers, or massive gas disks at galactic centers (Merritt & Milosavljevic 2005; Colpi & Dotti 2011, and references therein). The strong gravitational wave (GW) radiations from the coalescence of SMBHBs are the main targets of the GW detector Laser Interferometer Space Antenna (LISA) and the GW detecting program Pulsar Timing Array (PTA).

Spatially resolved dual or binary active galactic nuclei (AGNs) at kpc -scale separation were discovered in the past decade first in a few merging galaxy systems (e.g. Komossa 2003, 2006; Green et al. 2010), and recently in a large sample of AGNs showing double-peak narrow emission lines (Zhou et al. 2004; Xu & Komossa 2009; Comerford et al. 2009; Wang et al. 2009; Liu et al. 2010a; Smith et al. 2010; Liu et al. 2010b; Fu et al. 2010; Shen et al. 2011; Rosario et al. 2011). Meanwhile, more compact or hard SMBHBs are extremely difficult to observe with present telescopes (see Rodriguez et al. 2006, for the only pc -scale SMBHB candidate so far discovered by VLBA), and for sub- pc SMBHBs only indirect observational evidences are suggested in a few sub-classes of AGNs with peculiar radio morphologies (Begelman, et al. 1980; Liu 2004; Liu & Chen 2007), periodic variabilities (Sillanpaa et al. 1988; Valtaoja et al. 2000; Liu et al. 1995, 1997, 2006; Liu & Wu 2002), or special broad-emission-line features (Stockton & Farnham 1991; Gaskell 1996; Boroson & Lauer 2009). Although it is still unclear how SMBHBs can pass through the final pc -scale and become merged, some observations of AGNs and QSOs are suggested to be due to the coalescence of SMBHBs, e.g. the interruption and restarting of jet activities in double-double radio galaxies (Liu et al. 2003), and the rapid jet reorientation in X-shaped radio sources (Merritt & Ekers 2002; Zier 2005). For SMBHBs in quiescent galaxies some observational signatures have been predicted (Chen et al. 2008, 2009, 2011; Komossa & Merritt 2008b; Liu et al. 2009) but need to be confirmed observationally. Among all the observational evidences for the coalescence of SMBHBs in AGNs, X-shaped radio source is one of the most popular. X-shaped radio sources are a subclass of double-lobed radio sources, consisting of a pair of long and diffusive inactive “wings” oriented at a large angle relative to the active lobes (Leahy & Williams 1984; Dennett-Thorpe et al. 2002). The “spin flip model” suggests that the wings are the fossil plasma of old lobes and jets are misaligned with the wings because of swift jet reorientation due to the spin-flip of jet-ejecting SMBHs during the coalescence of SMBHBs (Merritt & Ekers 2002). Meanwhile, many other formation scenarios, which do not require binary black hole coalescence, are also proposed in the literature, including

merger of two jet-emitting AGNs (Lal & Rao 2007), hydrodynamic interaction between jet and intra-/inter-galactic medium (Wirth et al. 1982; Leahy & Williams 1984; Worrall et al. 1995; Capetti et al. 2002; Zier 2005; Saripalli & Subrahmanyam 2009; Hodges-Kluck et al. 2010), and precession of jet axis (Ekers et al. 1978; Begelman, et al. 1980; Liu 2004).

Numerical simulations show that the coalescence of two black holes not only leads to a spin-flip black hole but also to a kick of the post-merger black holes due to the anisotropic emissions of gravitational waves. Therefore, it is expected that the coalescence of SMBHBs in spin-flip radio sources should lead to the recoiling of post-merger SMBHBs surrounded by accretion disk. The recoiling velocity depends on the angular momentum and mass ratio of the pre-merger SMBHBs, and can be as large as 175 km s^{-1} for Schwarzschild black holes (Gonzalez et al. 2007), 3800 km s^{-1} for extremely spinning equal-mass black hole binaries with anti-aligned spin angular momenta in the orbital plane (Pretorius 2005; Herrmann et al. 2007; Baker et al. 2006, 2008; Campanelli et al. 2006, 2007a,b), or even 10^4 km s^{-1} in hyperbolic encounters (Healy et al. 2009). The gravitational recoiling SMBHBs in AGNs may lead to signatures such as kinematic and spatial offsets (Bonning et al. 2007; Komossa et al. 2008; Shields et al. 2009b; Civano et al. 2010; Robinson et al. 2010; Tsalmantza et al. 2011; Eracleous et al. 2011; Madau & Quataert 2004; Magain et al. 2005; Loeb 2007; Batcheldor et al. 2010; Jonker et al. 2010; Blecha & Loeb 2008; Guedes et al. 2009; Civano et al. 2010; Guedes et al. 2011; Blecha et al. 2011), along with some other electromagnetic signatures (see Komossa 2010, for a review).

In the following, we refer to the radio sources with spin-flip signatures, such as those in X-shaped radio sources, as “spin-flip radio sources”. In this paper, we adopt the spin-flip model and investigate the spectral and spatial signatures of the recoiling SMBHBs in such objects, using the empirical formula obtained in numerical relativity to calculate the spin angular momentum and recoiling velocity of the post-merger black hole. We neglect the slow precession of the spin axes of SMBHBs during the in-spiraling of SMBHBs. We assume that the old and active jets, respectively, form along the spin axes of the primary and post-merger SMBHBs and any jet-ejecting SMBHB has spin parameter $a = cS/GM^2 \geq 0.9$, where S is the black hole spin angular momentum, M is the black hole mass, G is the gravitational constant, and c is the speed of light. For the secondary SMBHB, no constraint on the spin parameter a_2 can be given. We assume that a_2 can be any value between 0 and 1 of flat probability distribution. Our results show that the SMBHBs producing detectable spin-flip angles should form in major mergers with mass ratio $\gtrsim 0.2$ – 0.3 and that the recoiling SMBHBs preferentially move in a direction with an angle $\lesssim 40^\circ$ relative to jet orientation. We calculate the Doppler kinematic shift of broad emission lines, the AGN off-center displacement in host galaxy, and the effects of recoiling SMBHBs on dust torus in spin-flip radio galaxies and quasars as a function of apparent jet reorientation angle and jet size. We finally collect a sample of 19 X-

shaped radio objects and calculate the detection probabilities for the proposed observational signatures.

The paper is organized as follows. In Section 2, we introduce the empirical formula for the spin angular momenta and the recoiling velocity of post-merger SMBHs obtained in numerical relativity. Section 3 describes our numerical simulations and general results for spin-flip radio sources. We collect a sample of 19 X-shaped radio objects and calculated the observational signatures of recoiling SMBHs in Section 4. Our discussions and conclusions are given in Section 5. Throughout the paper, we assume a Λ CDM cosmology with parameters $H_0 = 73 \text{ km s}^{-1} \text{ Mpc}^{-1}$, $\Omega_\Lambda = 0.73$, and $\Omega_m = 0.27$.

2. Empirical formula for spin angular momenta and recoiling velocities of post-merger SMBHs

It is shown that the final spin and the recoiling velocity of a post-merger SMBH can be calculated in high precision with the empirical formula fitting the simulation results of numerical relativity. Following Rezzolla et al. (2008), the final spin angular momentum \mathbf{S}_{fin} of a post-merger SMBH can be approximated as the sum of the two initial spin angular momenta \mathbf{S}_1 and \mathbf{S}_2 of the primary and secondary SMBHs, respectively, and a third vector $\tilde{\ell}$,

$$\mathbf{S}_{\text{fin}} = \mathbf{S}_1 + \mathbf{S}_2 + \tilde{\ell}, \quad (1)$$

where $\tilde{\ell}$ is the difference between the orbital angular momentum \mathbf{L} at large SMBHB separation and the angular momentum \mathbf{J}_{rad} radiated away during merger

$$\tilde{\ell} = \mathbf{L} - \mathbf{J}_{\text{rad}}. \quad (2)$$

Equation (1) can be written as

$$\mathbf{a}_{\text{fin}} = \frac{1}{(1+q)^2} (\mathbf{a}_1 + \mathbf{a}_2 q^2 + \ell q) \quad (3)$$

(Rezzolla et al. 2008), where mass ratio $q = M_2/M_1 \leq 1$, spin parameter vector $\mathbf{a}_{\text{fin}} = \mathbf{S}_{\text{fin}}/M^2$, $\ell = \tilde{\ell}/(M_1 M_2)$, the primary SMBH spin parameter vector $\mathbf{a}_1 = \mathbf{S}_1/M_1^2$, and the secondary SMBH spin parameter vector $\mathbf{a}_2 = \mathbf{S}_2/M_2^2$. M , M_1 , and M_2 are, respectively, the masses of the final SMBH, the primary SMBH, and the secondary SMBH. Here and in section (2), we use the natural units $G = c = 1$. In equation (3), the direction of the angular momentum vector ℓ is nearly parallel to the orbital angular momentum and its norm is

$$|\ell| = \frac{s_4}{(1+q^2)^2} (|\mathbf{a}_1|^2 + |\mathbf{a}_2|^2 q^4 + 2|\mathbf{a}_1|^2 |\mathbf{a}_2|^2 q^2 \cos \alpha) +$$

$$\left(\frac{s_5\eta + t_0 + 2}{1 + q^2}\right) (|\mathbf{a}_1| \cos \beta + |\mathbf{a}_2| q^2 \cos \gamma) + 2\sqrt{3} + t_2\eta + t_3\eta^2, \quad (4)$$

where s_4, s_5, t_0, t_2 , and t_3 are the empirical fitting coefficients given by Rezzolla et al. (2008), η is the symmetric mass ratio $\eta \equiv M_1 M_2 / (M_1 + M_2)^2 = q / (1 + q)^2$, and the three projected (cosine) angles α, β and γ are defined with the inner products

$$\cos \alpha \equiv \hat{\mathbf{a}}_1 \cdot \hat{\mathbf{a}}_2, \quad \cos \beta \equiv \hat{\mathbf{a}}_1 \cdot \hat{\ell}, \quad \cos \gamma \equiv \hat{\mathbf{a}}_2 \cdot \hat{\ell}. \quad (5)$$

In the definition of ℓ , the orbital angular momentum \mathbf{L} is the one at large (infinity) separation. In the calculation, we neglect the slow precession of spin axis around total angular momentum and use all the empirical formula for a finite separation $\gg M$ to calculate the spin-flip angle. We expected that this approximation can give good enough results to describe the jet reorientations in X-shaped radio sources.

Coalescence of SMBHBs not only leads to the spin-flip but also to a fast recoiling of the post-merger SMBH. The recoiling velocity of post-merger SMBH can be empirically given by

$$\mathbf{V} = V_m \mathbf{e}_1 + V_{\perp s} (\cos \xi \mathbf{e}_1 + \sin \xi \mathbf{e}_2) + V_{\parallel s} \mathbf{e}_3, \quad (6)$$

$$\begin{aligned} V_m &= A\eta^2 \sqrt{1 - 4\eta(1 + B\eta)}, \\ V_{\perp s} &= H \frac{\eta^2}{(1 + q)} \left(a_1^{\parallel} - q a_2^{\parallel} \right) \end{aligned} \quad (7)$$

(Campanelli et al. 2007a; Gonzalez et al. 2007), where \mathbf{e}_1 and \mathbf{e}_3 are, respectively, the unit vectors in the directions of the binary separation from the primary to the secondary black hole and the orbital rotating axis just before merger, and the unit vector $\mathbf{e}_2 \equiv \mathbf{e}_1 \times \mathbf{e}_3$. The index \parallel and \perp refer to, respectively, the projections of the vectors parallel and perpendicular to the orbital axis. The index m indicates the recoil velocity of unequal mass contribution, and s indicates the contribution due to spin. The fitting parameter ξ is the angle between the recoiling velocities in the orbital plane due to the mass asymmetry and spin angular momenta and we use $\xi = 145^\circ$ in the following calculations as in Lousto & Zlochower (2008). The fitting coefficients A, B , and H are taken from Campanelli et al. (2007a). For the kick velocity parallel to orbital axis, we use the empirical formula given by van Meter et al. (2010). These formula are equivalent to one suggested by Lousto et al. (2010a) if angular parameters are suitably interpreted. In order to use these formula for statistical calculation, we combined the equations (7), (8) and (9) in van Meter et al. (2010) and adopted the interpretation of angular parameters from Lousto et al. (2010a). Then we obtained the following formula

$$V_{\parallel s} = -\frac{K_2\eta^2 + K_3\eta^3}{q + 1} |a_1^{\perp} - q a_2^{\perp}| \cos(\Theta_{\Delta} - \Theta_0)$$

$$+ \frac{K_S(q-1)\eta^2}{(q+1)^3} |a_1^\perp + q^2 a_2^\perp| \cos(\Theta_S - \Theta_1), \quad (8)$$

where K_2 , K_3 , and K_s are fitting parameters taken from van Meter et al. (2010). In equation (8), a_i^\perp is the magnitude of the spin parameter vectors \mathbf{a}_i of the i th black hole projected into the orbital plane, Θ_Δ (Θ_S) is the angle between the in-plane component of $\Delta \equiv \mathbf{S}_2/M_2 - \mathbf{S}_1/M_1$ ($\mathbf{S} \equiv \mathbf{S}_1 + \mathbf{S}_2$) and the unit separation vector from the primary toward the secondary at merger and Θ_0 (Θ_1) is the corresponding initial value of Θ_Δ (Θ_S) at the arbitrary separation of the binary with quasi-circular orbit.

3. Numerical Simulations and Results

3.1. Monte Carlo simulations

With the empirical formula given in Section 2, we now investigate the distributions of the SMBH mass ratio, spin-flip angle, recoiling velocity in spin-flip radio sources under the spin-flip model. In our calculations, the physical quantities are specified in the Cartesian coordinate system defined by \mathbf{e}_1 , \mathbf{e}_2 , and \mathbf{e}_3 and so that the positive direction of the z -axis align with the orientation of \mathbf{e}_3 and the orbital plane of the pre-merger SMBHB is in the x - y plane. To calculate the final spin vector \mathbf{a}_{fin} and the recoiling velocity \mathbf{V} for a post-merger SMBH, we have to specify the following physical quantities of the pre-merger SMBHB: q , Θ_Δ , Θ_S , Θ_0 , Θ_1 , and both the magnitude and orientation of \mathbf{a}_1 and \mathbf{a}_2 . We employ the Monte Carlo scheme to generate these quantities according to the statistical properties motivated by the physical considerations. The details are as follows.

The mass ratio q of the SMBHB has a uniform distribution in the range $[0, 1]$, and the spin vectors \mathbf{a}_1 and \mathbf{a}_2 are randomly oriented (unless otherwise noted). Following Lousto et al. (2010a) and for statistical purpose, in the simulations we define Θ_Δ and Θ_S with respect to \mathbf{e}_1 , and take $\Theta_0 = 0$, Θ_1 has a uniform distribution in the range $[0, 2\pi]$. In the case of an spin-flip radio source, although both SMBHs before merger could be the candidates for the jet-ejecting black holes, we assume that the low luminosity diffusive lobes are produced by the primary SMBH before coalescence and the active jets form along the final spin axis of the post-merger SMBH. Because we are interested in radio loud AGNs or quasars with powerful relativistic jets both before and after the merger, we do simulations only for uniform distributions of a_1 within the range $0.9 \leq a_1 \leq 0.998$. For the spin of the secondary SMBH, we cannot give any priori constraint on it thus we assume a uniform distributions in the range of $0 \leq a_2 \leq 0.998$. Among the simulations, we adopt only those corresponding to $0.9 \leq a_{\text{fin}} \leq 0.998$ as the final results for spin-flip radio sources. Although we set an upper limit 0.998 rather than the extreme spin $a = 1$ to all the spin parameters by

physical consideration, our results are not significantly changed by this small difference in upper limit because of the regularity of the results and the rarity of SMBH merger at $a = 1$.

In each run of Monte Carlo simulations, we first draw a set of physical quantities according to the distribution functions specified above, and then calculate \mathbf{a}_{fin} and \mathbf{V} , using the equations (3)-(8). To derive the distribution functions of the physical quantities, we use 10^7 – 10^9 sets of the quantities, depending on the request of resolution. To compare the numerical results with the real observations, we project the vectors \mathbf{a}_{fin} and \mathbf{V} both along and vertical to the line of sight (LOS) vector \mathbf{e}_s , which is assumed to randomly orient. We calculate the angles w_1 and w_2 , respectively, between \mathbf{a}_1 and \mathbf{e}_s and between \mathbf{a}_{fin} and \mathbf{e}_s , which may be observed directly or observationally constrained. Because we assume that jets form along the spin axes of the primary SMBHs before merger and of the final SMBHs after merger, the spin flip during merger leads to the reorientation of jets. We also calculate the projected (apparent) jet reorientation angle δ , i.e. the angle between the components of \mathbf{a}_1 and \mathbf{a}_{fin} projected vertically to LOS

$$\cos(\delta) = \frac{(\mathbf{a}_1 \times \mathbf{e}_s) \cdot (\mathbf{a}_{\text{fin}} \times \mathbf{e}_s)}{|\mathbf{a}_1 \times \mathbf{e}_s| |\mathbf{a}_{\text{fin}} \times \mathbf{e}_s|}. \quad (9)$$

To be identified as a spin-flip radio source, both the active jets forming along the spin axis of the post-merger SMBH and the relic jets forming along the spin axis of the pre-merger primary SMBH should be resolvable by radio telescopes. Moreover, the active jets should orient at a large angle with respect to the relic jets. In the special case of X-shaped radio sources, the length of the relics jets (wings) should be at least 80% of the length of the active ones, and the angle between relic and active jets should exceed 15° (Leahy & Parma 1992). The requirements of length and symmetry imply that the angle between relic jets and LOS cannot be very small, and clear identification of diffusive extended wings from the plasma cocoon of active jets also requires a large relative angle between the projected wings and active lobes in the plane of the sky. Therefore, the simulations resulting in $w_1 < 20^\circ$ or $\delta < 15^\circ$ are not included in the later statistical analysis. Besides, a radio source would be observed as a blazar if the relativistic jet is nearly along the line of sight and the relativistic beaming effect becomes dominant. Resolving active jets and good measurement of their length and orientation therefore require that w_2 cannot be very small. For this reason, the simulations resulting in $w_2 < 10^\circ$ are excluded.

After excluding the solutions of the equations which do not fulfill the above selection criteria, only about 10^5 – 10^6 simulations are left and will be used in the derivation of the distribution functions of the SMBH mass ratio q , the spin flip angle Δ , and recoiling velocity \mathbf{V} for different apparent jet reorientation angles δ , and in the investigation of the effects of recoiling velocity on dust torus. To analyze the standard deviation of a distribution function,

we run in total 5 sets of Monte Carlo simulations.

3.2. Distributions of SMBH mass ratios in Spin-flip radio sources

Our results of the distribution of SMBH mass ratio q in the simulated spin-flip radio sources are shown in Figure 1. We calculate the apparent jet reorientation angle using Equation (9) and divide the simulation results into three groups, based on the apparent jet reorientation angles for $15^\circ < \delta < 40^\circ$, $40^\circ < \delta < 60^\circ$, and $65^\circ < \delta < 90^\circ$. Given the conditions we have, the mass ratio q in spin-flip radio sources cannot be uniquely determined, therefore we are able to give only the statistical probability $q(dP/dq)$ of a certain mass ratio, as the distribution function in Figure 1.

Our results imply that to form a detectable apparent jet reorientation angle with $\delta \geq 15^\circ$, the mass ratio of the SMBHB must be larger than 0.05, which is smaller than the minimum mass ratio obtained by Hughes & Blandford (2003). This difference of the minimum mass ratio is due to the projection effects on the spin flip which can amplify a small jet reorientation angle. If we set smaller lower limits on w_1 and w_2 , the amplification effect becomes more significant and we may get an even smaller minimum mass ratio. Our results also show that for a larger apparent jet reorientation angle the needed minimum mass ratio becomes larger. To form spin-flip radio structure with apparent jet reorientation angle $40^\circ < \delta < 60^\circ$, the needed minimum mass ratio is $q_{\min} \simeq 0.1$, while for $65^\circ < \delta < 90^\circ$, $q_{\min} \simeq 0.15$.

Figure 1 showed that for an spin-flip radio source with apparent jet reorientation angle $15^\circ < \delta < 40^\circ$, the SMBHB most probably has mass ratio $q \sim 0.3$, and large contribution comes from SMBHBs with mass ratio $0.15 \lesssim q \lesssim 0.5$ although the contribution from SMBHBs with $q \gtrsim 0.5$ cannot be completely neglected. For spin-flip radio sources with larger apparent jet reorientation angles, the contribution of the mergers of SMBHBs with larger mass ratio q become more significant while that of SMBHBs with smaller mass ratio becomes less important. For spin-flip radio sources with intermediate apparent jet reorientation angle $40^\circ < \delta < 60^\circ$, the mergers of SMBHBs with mass ratio $q \gtrsim 0.25$ may make significant contributions, although the contribution from SMBHB mergers with $q \sim 0.5$ is at local minimum. For $65^\circ < \delta < 90^\circ$, the jet reorientation in spin-flip radio sources is likely due to the merger of SMBHBs with mass ratio $q \gtrsim 0.35$, the larger the mass ratio, the more likely, and the largest contribution is due to the mergers with $q \gtrsim 0.6$. We notice that for $65^\circ < \delta < 90^\circ$ the typical probability $q(dP/dq)$ could be larger than unit although the integrated probability is unit. This is due to the reason that the probability per unit mass ratio varies very rapidly on a length scale much less than the typical mass ratio or $P/(dP/dq) \ll q$ for $q \gtrsim 0.8$.

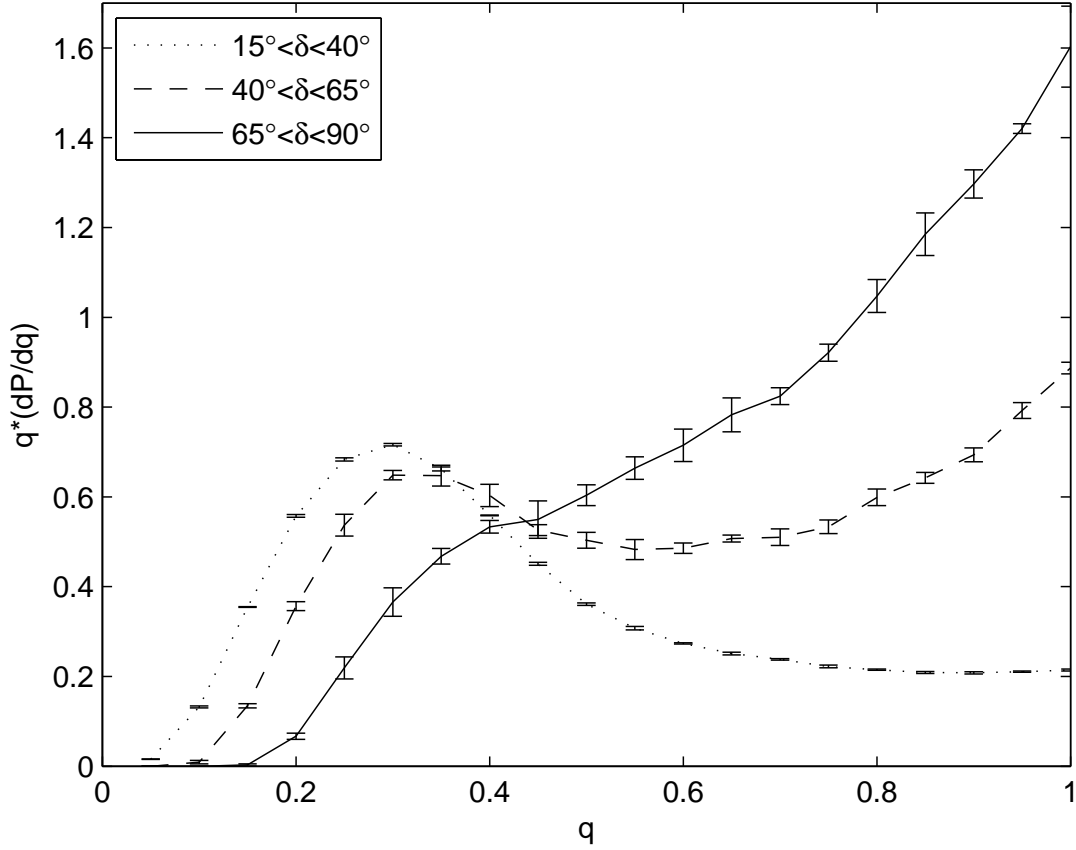


Fig. 1.— Distribution function of SMBHB mass ratio q in spin-flip radio sources for different apparent jet reorientation angles δ . Apparent jet reorientation angle δ is the angle between the orientations of the active and remnant (wings) jets, which is also the projected angle between the spin axes of the primary and the post-merger SMBHs. The minimum mass ratios depend on δ and are, respectively, $q_{\min} \simeq 0.05$ for $15^\circ < \delta < 40^\circ$, $q_{\min} \simeq 0.1$ for $40^\circ < \delta < 65^\circ$, and $q_{\min} \simeq 0.15$ for $65^\circ < \delta < 90^\circ$. SMBHBs in most spin-flip radio sources have mass ratio $q \gtrsim 0.3$ and thus are formed by major mergers. Error bar gives 1σ standard error.

3.3. Spin flip angles and recoiling velocities of post-merger SMBHBs

Our results suggest that the merger of SMBHB with a given mass ratio can lead to apparent jet reorientation angle δ in a broad range, which is partially due to the projection effect. In this section, we show the distribution function of the intrinsic spin flip angle Δ . We calculate Δ using the relation $\cos(\Delta) = \mathbf{a}_1 \cdot \mathbf{a}_{\text{fin}} / |\mathbf{a}_1| |\mathbf{a}_{\text{fin}}|$ and give the results for typical mass ratios $q = 0.3$, $q = 0.7$, and $q = 1$ in the left panel of Figure 2. In the same panel, we also give the distribution of Δ in minor merger $q = 0.1$, which is also the lower mass ratio limit to form spin-flip radio sources with moderate apparent jet reorientation angles.

We can see that in spin-flip radio sources the typical spin flip angle corresponding to the maximum probability increases with mass ratio q from $\Delta = 12^\circ$ for minor merger $q = 0.1$, $\Delta = 19^\circ$ for major merger $q = 0.3$, and $\Delta = 25^\circ$ for major merger $q = 0.7$ to $\Delta = 30^\circ$ for equal-mass merger $q = 1$. Our results also show that the spin flip angle Δ has a broad distribution and the full width at half maximum $\text{FWHM}(\Delta)$ also increases with SMBHB mass ratio from $\text{FWHM}(\Delta) \simeq 7^\circ$ for minor merger $q = 0.1$ through $\text{FWHM}(\Delta) \simeq 13^\circ$ for major merger $q = 0.3$ to $\text{FWHM}(\Delta) \simeq 28^\circ$ for equal-mass merger $q = 1$. For equal-mass mergers ($q = 1$), we find $\Delta \lesssim 55^\circ$. The trial solutions with $\Delta > 55^\circ$ are mostly rejected because that significant spin down of the post-merger SMBH would occur.

The maximum spin flip angle for minor merger $q = 0.1$ is about 15° , which is consistent with the results given in Figure 1 in which no spin-flip radio source with apparent jet reorientation angle $\delta > 40^\circ$ results from minor merger with $q = 0.1$. However in Figure 1, some spin-flip radio sources with apparent jet reorientation angle $15^\circ < \delta < 40^\circ$ are from the minor merger with $q = 0.1$, this is because of the projection amplification. Comparing Figure 1 and Figure 2, one can see that the projection amplification becomes more important for larger apparent jet reorientation angle. For mergers with $q = 0.3$, the maximum intrinsic spin flip angle is $\Delta < 30^\circ$ in Figure 2, but in Figure 1 a significant fraction of spin-flip radio sources with apparent jet reorientation angle $40^\circ < \delta < 65^\circ$ are due to these mergers and even their contributions to the formation of spin-flip radio sources with $65^\circ < \delta < 90^\circ$ are not negligible because of the projection amplifications. The amplification effect becomes dominant for the formation of spin-flip radio sources with $65^\circ < \delta < 90^\circ$, because Figure 2 showed that even for equal-mass mergers $q = 1$ the probability to have spin flip angle larger than 60° is nearly zero.

It has been suggested that the spins of SMBHBs may be partially aligned via interactions with a gas disk or via GR precession (Bogdanović et al. 2009; Dotti et al. 2009; Kesden et al. 2010) prior to the binary coalescence. To understand the effects of spin alignment on the distribution of spin-flip angle, we ran test simulations assuming that the black hole spins are initially partially aligned within 30° relative to the orbital angular momentum of SMBHB

(also assumed by Lousto et al. 2010a). The corresponding results are shown in the right panel of Figure 2. We did not consider further alignment within 10° , because such extreme alignment hardly ever produces an apparent spin-flip angle greater than 15° , the minimum angle required to identify spin flip in radio sources. When spin alignment is taken into account, the peaks of the distribution functions move systematically to lower Δ and the FWHMs shrink significantly. The maximum intrinsic spin-flip angle, $\sim 30^\circ$, is achieved when $q = 1$. These results imply that in the context of spin-flip model, radio sources with spin-flip angles much greater than $\sim 30^\circ$ are strong evidences against spin alignment during SMBHB coalescence.

While the spin axis of jet-ejecting SMBHs reorient during the merging of SMBHBs, the post-merger SMBHs get kicked due to the anisotropic radiation of gravitational wave. In the upper panel of Figure 3, we give the distribution of the recoiling velocity V in spin-flip radio sources for black holes with random initial spin orientation and typical mass ratios $q = 0.3, 0.7$, and 1 , which are, respectively, the typical mass ratios in spin-flip radio sources with apparent jet reorientation angles $15^\circ < \delta < 40^\circ$, $40^\circ < \delta < 65^\circ$, and $65^\circ < \delta < 90^\circ$. Our results show that mergers of SMBHBs with larger mass ratios could lead to larger recoiling velocities with broader distributions. For major mergers of $q = 0.3$, the recoiling velocities show a distribution ranging from nearly 0 km s^{-1} to larger than 1200 km s^{-1} with a most possible velocity 600 km s^{-1} . For major mergers of $q=0.7$ or $q=1$, the recoiling velocities V show broader distributions ranging from nearly 0 to larger than 2100 km s^{-1} . The most probable kick velocity is about 900 km s^{-1} , while the typical probability for a post-merger SMBH to have recoiling velocity larger than 1000 km s^{-1} is nearly 50 percent. In Figure 3, we also give the results for minor mergers with $q = 0.1$, which will lead to small spin flip of $\Delta \leq 16^\circ$. The kicked SMBHs for $q = 0.1$ have with a very narrow velocity range with $\text{FWHM}(V) \simeq 210 \text{ km s}^{-1}$ and the most probable kick velocity is 150 km s^{-1} . Therefore, our results suggest that the post-merger SMBHs in spin-flip radio sources with larger apparent jet reorientation angle should have larger recoiling velocities, in particular for spin-flip radio sources with $15^\circ < \delta < 40^\circ$ the typical recoiling velocity is about 600 km s^{-1} , while for spin-flip radio sources with $65^\circ < \delta < 90^\circ$ the recoiling velocity is typically about 900 km s^{-1} or larger. If pre-merger spin alignment is considered, the typical spin-flip angle would be smaller than 30° according to the right panel of Figure 2. The typical recoiling velocity would be significantly smaller, as the thin dashed line shows in the upper panel of Figure 3.

In addition to the magnitude, it is also important to know the direction of the recoiling velocity of a kicked SMBH. In the lower panel of Figure 3, we give the distribution of the angle α of recoiling velocity relative to the spin axis of post-merger SMBH, or the orientation of the active jets. Our results suggest that the kicked SMBHs are inclined to move along the active jets and likely to avoid moving in the SMBHB orbital plane. Earlier statistical

studies by Lousto et al. (2010b) on the spin properties of merger remnants showed the similar trend and attributed the alignment to that both final spin and recoiling velocity are biased toward (counter-)aligning with the orbital angular momentum of the pre-merger SMBHB. This explanation implies that if the spin axes of SMBHs could align with the orientation of orbital angular momentum prior to coalescence, the bias would be even stronger and the correlation between the orientations of final spin and recoiling velocity would be tighter. The result from our test simulations with partial spin alignment, which is shown in the lower panel of Figure 3 as the thin dashed line, supports this implication. For major mergers with $q > 0.3$, most kicked SMBHs move in a direction within 40° with respect to the final spin axes or the active jets, which is about or less than the opening angle of the dust torus in AGN unification model. Therefore, recoiling SMBHs in most spin-flip radio sources do not move across the dust torus and make direct impact on it, if the active jets are vertical to the plane of the dust torus. For equal-mass mergers with $q = 1$, nearly all kicked SMBHs move in the direction $\alpha \sim 15^\circ$ anti-parallel to the final spin angular momenta. These results imply that if SMBHBs merge in blazars, the broad emission lines are nearly maximumly Doppler-shifted for a given recoiling velocity. For minor merger with $q = 0.1$, the kicked SMBHs move in a broad range of directions and most of them move in the direction of about 50° relative to the active jets.

3.4. Line-of-sight velocities and apparent off-center displacements of recoiling AGNs

The projections of spin flip angles vertical to LOS is the apparent jet reorientation angles δ of spin-flip radio sources and can be given by observations. The projected components V_{\parallel} of recoiling velocities along LOS can produce Doppler-shifted kinematic offsets of broad emission lines with respect to the narrow emission lines of AGNs or to the spectral lines of host galaxies, while the other projected component V_{\perp} perpendicular to LOS leads to apparent spatial offsets of AGNs with respect to the center of the host galaxies. Therefore, in this section we investigate the Doppler-shifting recoiling velocity V_{\parallel} and the apparent spatial off-center displacement L_{\perp} of recoiling SMBHs as a function of the apparent jet reorientation angle in spin-flip radio sources. To take into account the deceleration of a recoiling SMBH due to dynamical friction against stars in the host galaxy and dark matter in the halo, we adopted an 1-D analytic model (see Appendix A) to calculate V_{\parallel} and L_{\perp} as a function of t_e , the elapsed time since a post-merger SMBH gets kicked.

Armitage & Natarajan (2002) showed that the merger of SMBHB in an AGN would truncate the inner accretion disk, and Liu et al. (2003) suggested that the jet formation

will be interrupted accordingly and later restart, when the inner disk is refilled after an interruption timescale t_{tr} . In this scenario, the total elapsed time after the SMBHB coalesces is the sum of t_{tr} and the life time of the active jets t_a , i.e. $t_e = t_a + t_{\text{tr}}$. In X-shaped radio sources, one can estimate the radiation ages t_{ra} of active radio lobes using radiation models for relativistic electron plasma in the radio lobes, or calculate the dynamic lifetime t_{dy} of jets using the typical length of jets L_a and the typical advancing velocity V_{hs} of hot-spots in the active radio lobes (e.g. Alexander & Leahy 1987). We can use either of them as the typical lifetime t_a of active jets. To calculate t_{tr} , we adapted the equation (10) in Liu et al. (2003), $t_{\text{tr}} \simeq 4 \times 10^3 q^{3/5} (M/10^8 M_\odot) \text{ yr}$, for SMBHBs with circular orbit¹ and assumed a viscous parameter of 0.1 and an opening angle of 0.01 for a standard thin accretion disk. The resulting interruption timescale of jet formation for $M \lesssim 10^9 M_\odot$ is and much shorter than the typical lifetime of the active jets in a giant radio source (GRS, typical jet size ~ 100 kpc and age $\sim 3 \times 10^6 \text{ yr}$, e.g. § 4). However, in a compact steep-spectrum (CSS, typical jet size ~ 10 kpc and age $\sim 10^5 \text{ yr}$) or a gigahertz peaked-spectrum (GPS, typical jet size $\lesssim 1$ kpc and age $\lesssim 10^4 \text{ yr}$) radio source (O’Dea 1998), the interruption time t_{tr} become comparable or greater than the lifetime of the active jets (assuming $V_{\text{hs}} \simeq 0.3c$, Owsianik et al. 1999), thus not negligible in the calculation of t_e .

Radio sources are classified into radio galaxies and quasars. In the unification model of AGNs (Urry & Padovani 1995), radio quasars are those radio galaxies that the angles between the relativistic jets and LOS are small so that the accretion disks and the outer dust tori are nearly face on. Therefore, in quasars the broad emission line regions can be observed directly. However, in radio galaxies, the accretion disks and dust tori are nearly edge-on and the broad emission line regions are obscured by dust tori. The division viewing angle between radio quasars and galaxies is about 44.4° . In the following, we calculate the Doppler-shifting recoiling velocities and apparent spatial offsets for spin-flip radio galaxies with $44.4^\circ < w_2 < 90^\circ$ and for spin-flip quasars with $10^\circ < w_2 < 44.4^\circ$, respectively. We do not consider the cases with $w_2 < 10^\circ$ because such sources will be identified as blazars due to the close alignment of jets and LOS.

The upper panels of Figure 4 show the cumulative distributions of the LOS velocity V_{\parallel} in spin-flip quasars. In the calculation, we assumed a typical black hole mass of $10^8 M_\odot$ and stellar velocity dispersion of host galaxy 200 km s^{-1} . In the left panel, the solid curve refers to the initial kick velocity immediately after SMBHB coalescence, and the other curves refer to quasars with increasing jet sizes and ages, namely, GPSs, CSSs, and GRSs. With the increase

¹ In equation (10) of Liu et al. (2003) the factor $f = 21.8$ and the resonance number $n = 5$ are adopted for binary orbit with eccentricity $e = 0.68$. While, for a circular binary orbit which we assumed here, $f = 1$ and $n = 2$.

of time since kick and the transition of quasar types from GPSs to CSSs and finally GRSs, the deceleration of recoiling SMBH due to the dynamical friction against stars in the host galaxy and dark matter in the halo becomes more significant, so both the maximum V_{\parallel} and the probability for $V_{\parallel} > 10 \text{ km s}^{-1}$ decreases. For GRSs, the bump of the cumulative distribution function at $V_{\parallel} < 70 \text{ km s}^{-1}$ is contributed mainly by the SMBHs in the long-term oscillatory phase II (Gualandris & Merritt 2008). In the right panel, we show distribution functions of V_{\parallel} for CSS quasars with three different apparent spin-flip angles, i.e., $15^{\circ} < \delta < 40^{\circ}$, $40^{\circ} < \delta < 65^{\circ}$, and $65^{\circ} < \delta < 90^{\circ}$. The first distribution function for $15^{\circ} < \delta < 40^{\circ}$ resembles the distribution function for all CSSs shown in the left panel, indicating that the majority of the spin-flip CSSs have small δ . While the latter two distribution functions are significantly higher than the first one, implying that V_{\parallel} is generally larger for a spin-flip quasar with larger apparent jet reorientation angle. Current spectroscopy with medium resolution $R \simeq 1800$, such as that from Sloan Digital Sky Survey, can resolve a Doppler-shift velocity of $\Delta v \simeq 167 \text{ km s}^{-1}$ (Eracleous et al. 2011). A spectral resolution as high as 46,000, such as HIRES/Keck and UVES/VLT (Arav et al. 1998; Balashev et al. 2011), can even resolve $\Delta v \simeq 6.5 \text{ km s}^{-1}$. Therefore, with a conservative assumption of a spectral resolution of 200 km s^{-1} , the implications from the upper panels of Figure 4 are as follows. Among all quasars showing spin-flip signatures, the probability of detecting Doppler-shifted broad emission lines drops from as high as 50% for quasars with quenched jet formation and activity, to $\lesssim 20\%$ in GPS and CSS quasars, and to $\lesssim 2\%$ in GRSs. However, if only quasars with $\delta > 40^{\circ}$ are considered, the detection probability would rise by several times up to an order of magnitude. The above results also suggest that spin-flip quasars hardly ever have LOS velocities greater than 2000 km s^{-1} .

In the lower panels of Figure 4, we give the cumulative distribution functions of L_{\perp} , the apparent off-center displacement, for quasars with different typical jet sizes (*left*) and with different apparent spin-flip angles (*right*). As the jet size grows and deceleration proceeds, the maximum L_{\perp} increase while the probability for $L_{\perp} > 1 \text{ pc}$ decreases. The probability for a spin-flip quasar to have $L_{\perp} > 2 \text{ kpc}$ is negligible, therefore the recoiling quasar is confined in its host galaxy. We can also see that for quasars with larger δ , the probability of $L_{\perp} > 1 \text{ pc}$ is generally greater. To detect an off-center quasar, one needs to observe the angular offset between the recoiling SMBH and the center of its host galaxy. Using the images obtained with *Hubble Space Telescope* (*HST*) of spatial resolution about 100 milli arcsec (mas) and a relative astrometric accuracy $\sim 12 \text{ mas}$, Batcheldor et al. (2010) recently detected an angular displacement of $\sim 100 \text{ mas}$ between the SMBH and the photo-center center of host galaxy in M87. The detection implies that the relative angular astrometric accuracy of a telescope may be more important in observing off-center displacements of recoiling SMBHs. The current large telescopes, e.g. the Keck II telescope and *Very Large Telescope* (*VLT*) equipped with

adaptive optics (AO) systems, can achieve the highest angular resolution ~ 20 mas and relative astrometric accuracies ~ 0.2 mas at infrared wavelength (Wizinowich et al. 2000; Lu et al. 2010), while future astrometric interferometer missions, such as Gaia, are designed to achieve sub-mas resolution (e.g. Popovic et al. 2011). At a distance of 100 Mpc (1 Gpc), an angular displacement of 0.1 mas corresponds to a physical scale of 0.05 (0.5) pc. The lower panels of Figure 4 indicates that the probability with large telescopes with AO systems or Gaia detecting off-centered quasars among the spin-flip quasar sample is $\gtrsim 50\%$ ($\gtrsim 30\%$) for 0.05 (0.5) pc. In the GPS subsample, especially, the detection probability is 95% both for 0.05 pc and 0.5 pc.

Figure 5 shows the same distribution functions as in Figure 4, but for spin-flip galaxies. The distribution functions show similar dependence on typical jet size and apparent spin-flip angle as that in spin-flip quasars. However, due to the projection effect, the maximum and mean values of V_{\parallel} for spin-flip galaxies are smaller than those for spin-flip quasars, and the maximum and mean values of L_{\perp} are slightly greater.

The above results are derived assuming a black hole mass of $10^8 M_{\odot}$. The corresponding kick velocity for a recoiling SMBH to escape to the effective radius of the host galaxy is about 1600 km s^{-1} . For systems with larger (smaller) black holes, the escape velocity becomes higher (lower). As a result, given t_e , the probability of detecting either Doppler-shifted broad emission lines or off-center AGN displacement would decrease (rise). We did not consider spin alignment in this subsection, which (if taken into account) would reduce v_k and the possibilities of detecting appreciable V_{\parallel} or L_{\perp} . Since SMBHB coalescence with spin alignment hardly ever produces any radio source with $\Delta > 40^\circ$, radio sources showing large apparent spin-flip angles $\delta > 40^\circ$ are consistent with random spin orientation, and for these sources our conclusions are unchanged.

3.5. Truncation of dust torus and dust poor AGNs

The dust torus around central SMBH is an essential component in the unification model of AGNs. The inner edge of dust torus, $r_{\text{tor,in}}$, is most probably determined by the dust sublimation radius

$$r_{\text{tor,in}} \gtrsim 0.4 \left(\frac{L_{\text{bol}}}{10^{45} \text{ erg s}^{-1}} \right)^{1/2} \left(\frac{1500 \text{ K}}{T_{\text{sub}}} \right)^{2.6} \text{ pc} \quad (10)$$

(e.g. Nenkova et al. 2008), where L_{bol} is the AGN bolometric luminosity, and T_{sub} is the dust sublimation temperature. The outer radius of dust torus, $r_{\text{tor,out}}$, is poorly determined but likely not much larger than $r_{\text{tor,out}} \sim 20 r_{\text{tor,in}}$ (e.g. Elitzur 2007). Inside the dust torus is the

broad emission line region, the size of which can be given with the empirical scaling relation

$$r_{\text{BLR}} = 1.9 \times 10^{-2} \left[\frac{\lambda L_{\lambda}(5100\text{\AA})}{10^{44}\text{erg s}^{-1}} \right]^{0.69} \text{ pc}, \quad (11)$$

where $L_{\lambda}(5100\text{\AA})$ is the AGN luminosity at $\lambda = 5100\text{\AA}$ (Kaspi et al. 2005). The dichotomy of Type II and Type I quasars is then caused by whether or not LOS toward the broad line regions of AGNs is blocked by the dust tori.

Komossa & Merritt (2008a) showed that in a large fraction of recoiling quasars the matter in dust tori would become unbound to the recoiling SMBHs and the Type II quasars obscured by the dust tori would transform to unobscured Type Is. When a SMBH gets a kick velocity V , the matter orbiting the SMBH at radius $r \gtrsim r_k$ becomes unbound and only those with $r \lesssim r_k$ remains bound to the recoiling SMBHs. The critical radius is

$$r_k \simeq \frac{GM}{V^2} \approx 0.43 \left(\frac{M}{10^8 M_{\odot}} \right) \left(\frac{V}{10^3 \text{km s}^{-1}} \right)^{-2} \text{ pc}, \quad (12)$$

where M_{\odot} is the solar mass and M is the mass of kicked SMBH after merger. If V is larger than a critical value V_{cr} which satisfies $r_k = r_{\text{tor,in}}$, all the matter in dust torus becomes unbound, therefore the recoiling quasar must be “dust free”, and the initial radio galaxy will become an off-center quasar. If the recoiling velocity V is not only larger than V_{cr} but also

$$V_{\text{wl}} \simeq 4.8 \times 10^3 \left(\frac{M}{10^8 M_{\odot}} \right)^{1/2} \left[\frac{\lambda L_{\lambda}(5100\text{\AA})}{10^{44}\text{erg s}^{-1}} \right]^{-0.35} \text{ km s}^{-1}, \quad (13)$$

a part of the matter in broad line region may also become unbound and the recoiling quasar will become a weak emission line object. However, if the recoiling velocity is moderate and $V \lesssim V_{\text{dp}} \sim V_{\text{cr}}(r_{\text{tor,in}}/r_{\text{tor,out}})^{1/2}$, the critical radius r_k is larger than $r_{\text{tor,in}}$ but smaller than $r_{\text{tor,out}}$. Then part of the dust torus of the recoiling AGN will become unbound, and the object will become “dust poor”.

For a typical radio source of $M = 2 \times 10^8 M_{\odot}$, $T_{\text{sub}} = 1500\text{K}$, $f_{\text{tor}} = r_{\text{tor,out}}/r_{\text{tor,in}} \sim 20$, and $L_{\text{bol}} = 10^{45}\text{erg s}^{-1}$ or $\lambda L_{\lambda}(5100\text{\AA}) \simeq 10^{44}\text{erg s}^{-1}$, the critical recoiling velocity for the dust torus to be completely truncated and the object to become “dust free” is $V_{\text{cr}} = 1466\text{km s}^{-1}$. Meanwhile, the critical velocity for the dust torus to be truncated partially and the object to become “dust poor” is $V_{\text{dp}} \sim 300\text{km s}^{-1}$. Our calculations show that the probabilities for such a typical radio source to have velocity larger than the critical velocity V_{cr} are approximately 0.9% for $15^\circ < \delta < 40^\circ$, 11% for $40^\circ < \delta < 65^\circ$, and 10% for $65^\circ < \delta < 90^\circ$. Therefore, only about 10% of spin-flip radio sources with $\delta > 40^\circ$ will become “dust free” quasars or broad emission line radio galaxies if broad line regions are present. However, the critical velocity V_{dp} is at least two times smaller than the most-probable velocity in spin-flip

radio sources (c.f. Figures 1 and 3). Our calculations indicate that the probabilities for a typical spin-flip radio source to become “dust poor” are approximately 72% for $15^\circ < \delta < 40^\circ$, 85% for $40^\circ < \delta < 65^\circ$, and 85% for $65^\circ < \delta < 90^\circ$. Therefore, most spin-flip radio sources should be “dust poor”. To become a weak emission line quasar, the recoiling velocity in a typical spin-flip radio source should be $V \gtrsim V_{\text{wl}} \simeq 6.7 \times 10^3 \text{ km s}^{-1}$, which is larger than the maximum possible recoiling velocity produced during the merger of SMBHB with circular orbit. Since the bolometric luminosity L_{bol} should not greatly exceed the Eddington limit $\sim 10^{46} (M/10^8 \text{ M}_\odot) \text{ erg s}^{-1}$, equation (13) imposes a lower limit on V_{wl} for a given black hole mass, which is $\sim 9.5 \times 10^2 f_{\text{bol}}^{0.35} (M/10^8 \text{ M}_\odot)^{0.15} \text{ km s}^{-1}$, where $f_{\text{bol}} = L_{\text{bol}}/[\lambda L_\lambda(5100\text{\AA})]$ is the bolometric correction factor typically in the range $5 < f_{\text{bol}} < 20$ for AGNs. For less massive recoiling black holes, this lower limit would be smaller and more easily achievable. Therefore, weak-line AGNs, if exist, preferentially reside in AGNs with small black holes ($M \sim 10^6 \text{ M}_\odot$) and high luminosity.

4. Recoiling SMBHs in a sample of X-shaped radio objects

In section 3, in order to investigate the distributions of V_{\parallel} and L_{\perp} for spin-flip radio sources, we have to specify the value or make assumptions for the distributions of the unknowns, such as q , \mathbf{a}_1 , \mathbf{a}_2 , \mathbf{a}_{fin} , t_a , δ , w_2 , etc. However, for a real X-shaped radio object, constraints on the distributions of several unknowns can be made by observations. For example, according to section 3.2, the formation of X-shaped radio feature requires mass ratio $q \gtrsim 0.1$ and most probably $q \gtrsim 0.2$. The fact that X-shaped sources are radio loud AGNs implies $a_1 > 0.9$ and $a_{\text{fin}} > 0.9$. In this section, we study the conditional probability distributions of V_{\parallel} and L_{\perp} under more observational constraints for a sample of real X-shaped radio objects.

4.1. The sample of X-shaped radio objects

Mezcua et al. (2011) studied a sample of 29 X-shaped radio objects, which is drawn from the list of 100 X-shaped radio source candidates (Cheung 2007). They estimated for their sample objects the dynamic ages of the active radio lobes and the central black hole masses. The central black hole masses are computed with the empirical relationships either between SMBH mass and the stellar velocity dispersion of host galaxy, or between the width of broad emission line and optical luminosity $\lambda L_{5100\text{\AA}}$ at $\lambda = 5100\text{\AA}$. Landt et al. (2010) studied the optical spectra of another sample of X-shaped radio objects and estimated the viewing angles w_2 of the active jets, based on the relationship between the viewing angles and

the rest frame equivalent widths of the narrow emission lines O III $\lambda 5007$ and O II $\lambda 3727$. We cross-identified the two samples of X-shaped radio objects and obtained 23 objects to constitute our sample of X-shaped radio objects for further study.

We read the viewing angles w_2 for the 23 X-shaped radio sources from the Figure 1 of Landt et al. (2010) in which they divided the objects into four groups according to $0^\circ < w_2 < 15^\circ$, $15^\circ < w_2 < 35^\circ$, $35^\circ < w_2 < 60^\circ$, and $60^\circ < w_2 < 90^\circ$. We will follow the division of the objects because of the large uncertainties in the estimations of the viewing angles. In Landt et al. (2010), a few of our sample objects were classified into the group of $60^\circ < w_2 < 90^\circ$, while upper limits, $w_2 \lesssim 70^\circ$, were presented in their plot. Therefore, we assign these objects in a range of $45^\circ < w_2 < 70^\circ$ in our calculations.

We measured the apparent jet reorientation angles δ , the angle between the orientations of active lobes and wings, of the 23 X-shaped radio objects from the radio images given by Lal & Rao (2007) for 3C192, 4C+32.25, 4C+48.29, 1059+169, and 3C223.1, by Wang et al. (2003) for 4C+01.30, and by Cheung (2007) for the rest 17 objects. To do the measurement, we have to define the orientations of the active lobes and the wings. The orientation of active lobes is defined with the line passing through the center of the host galaxy and the hot spots inside the active radio lobes. However, it is very difficult to define the orientation of wings because they are very wide, diffusive, and without hot spots inside or central bright plasma jets along them. To overcome this problem, we define two orientations of the edges of a wing, both of which starting from the galactic center but one along the most furthest side (contour) and the other along the closest side (contour) of the wing with respect to the active jets. With the two orientations, we then measured two angles δ_1 and δ_2 between the orientations of active lobes and the two edges of wings, respectively, and took the mean value of δ_1 and δ_2 as the value of apparent jet reorientation angle δ . Because of the limited image quality, the obtained values for δ have very large uncertainties. We take 15° as the typical uncertainty for the measurement of δ , but for some objects the uncertainties are much larger. In particular, the uncertainties of δ for the objects J0813+4347, J1043+3131, J1111+4050, and J1210+1121 are extremely large, therefore these objects will not be included in our further calculations. Finally, our sample of X-shaped radio sources consists of 19 objects which are listed in Table 1.

In Table 1, Column 1 lists the IAU names of the objects based on the J2000.0 coordinates and other common catalog names, and Column 2 gives the spectroscopic identification as well as redshift, G for radio galaxies and Q for radio quasars. Columns 3, 4, 6, 7, and 8 are, respectively, the masses of central SMBHs, the optical luminosities of AGNs at 5100\AA , the viewing angles w_2 and the dynamic ages t_a of active lobes, and the references ($V_{\text{hs}} = 0.1c$ for GRSs is assumed in the reference literatures). In Column 5, we give the angles δ

between the active lobes and wings and the uncertainties measured in this paper. Column 9 gives the critical velocities in unit of 100 km s^{-1} for AGNs to become dust-free, calculated according to $r_k = r_{\text{tor,in}}$ and assuming $f_{\text{bol}} = 10$. Column 10 gives the critical velocities for AGNs to become dust-poor, calculated according to $r_k = r_{\text{tor,out}}$ and assuming that $f_{\text{tor}} = 20$. Column 11 is the viewing angles w_1 of the wings. Because w_1 cannot be constrained observationally and could be any value in the range of $20^\circ \lesssim w_1 \leq 90^\circ$, we considered three possible bins, namely $(20^\circ, 40^\circ)$, $(40^\circ, 60^\circ)$, and $(60^\circ, 90^\circ)$.

4.2. Spectral kinematic offsets and apparent spatial displacements

To compute the projected recoiling velocities along and vertical to LOS using Equations (3)-(8), we have to know the mass ratio q , spin vectors \mathbf{a}_1 and \mathbf{a}_2 , and the LOS vector \mathbf{e}_s for each object. From observations we can estimate only the quantities w_1 , w_2 , and δ , and may assume $a_1 > 0.9$ and $a_{\text{fin}} > 0.9$ as in section 3. For the mass ratio q , the results given in section 3.2 suggest that $q > 0.1$ and most probably $q > q_{\text{min}} \approx 0.2$. Therefore, we may put a lower limit for q in our simulations. Our simulations showed that different lower limits of mass ratio q do not change the conclusions significantly. We do not have any further knowledge of q , \mathbf{a}_1 , \mathbf{a}_2 and \mathbf{e}_s . Therefore, we assumed possible distributions of the quantities and used Monte Carlo simulations to generate their values. For simplicity, we assumed flat probability distributions of the parameters q with $q_{\text{min}} \leq q \leq 1$, a_1 with $0.9 \leq a_1 \leq 0.998$, and a_2 with $0 \leq a_2 \leq 0.998$. We also assumed random orientations of spin vectors \mathbf{a}_1 , \mathbf{a}_2 , and the LOS vector \mathbf{e}_s . Given \mathbf{a}_1 , \mathbf{a}_2 , and \mathbf{e}_s , we calculated w_1 , w_2 , and δ according to the relevant formula in section 2, and then we used the observed w_1 , w_2 , and δ given in Table 1 to select viable solutions for $(\mathbf{a}_1, \mathbf{a}_2, \mathbf{e}_s)$. Finally, given q , M , and t_a , we derive t_e according to the scheme explained in § 3.4, and then compute the decelerated LOS velocity V_{\parallel} and apparent off-center displacement L_{\perp} , using the 1-D analytical model described in Appendix A.

As in section 3, Monte Carlo simulations are carried out for each of the 19 X-shaped radio objects in our sample. We derived the probability distributions of Doppler-shifting recoiling velocity and apparent spatial off-center displacements in the objects, based on the 10^7 – 10^9 sets of trial solutions to the equations and excluding those which are inconsistent with the observational constraints. The final results are obtained with about 10^5 – 10^6 trial solutions. In our simulations for the objects J1101+1640, J1210-0341, J1327-0203, and J1444+4147, no trial solution of the equations (3)-(8) is found to fit all the observational conditions. This may imply that either our assumptions for the physical quantities are invalid or the spin-flip is not applicable for these objects. For the rest 15 objects in our sample, final solutions to

the equations can be obtained at least for one of the three bins of viewing angle, namely $20^\circ < w_1 < 40^\circ$, $40^\circ < w_1 < 60^\circ$, and $60^\circ < w_1 < 90^\circ$. The cumulative distributions of the LOS velocity V_{\parallel} and the apparent offset-center displacement L_{\perp} for the 15 objects are given in Figs. 6-8. Based on the cumulative distribution functions, we then derive the probability of displaying Doppler-shifted broad emission lines, $P_{v,\parallel}$, and off-center spatial displacements, $P_{\theta,\perp}$. These two probabilities are given, respectively, in Columns 12 and 13 of Table 1. The two values in Column 12, from left to right, correspond to $V_{\parallel} > 500 \text{ km s}^{-1}$ and $V_{\parallel} > 200 \text{ km s}^{-1}$, while the two values in Column 13 correspond to angular sizes $\theta_{\perp} > 10 \text{ mas}$ and $\theta_{\perp} > 0.1 \text{ mas}$.

The probability $P_{v,\parallel}$ for our sample of X-shaped radio sources is typically smaller than 10%, except for J0941-0143, 4C+01.30, J1348+4411, and J1614+2817. While $P_{v,\parallel}$ for the former three object are still smaller than 20%, the last object, J1348+4411, shows an appreciable probability ($\simeq 40\%$) of having $V_{\parallel} > 200 \text{ km s}^{-1}$. In the case of $P_{\theta,\perp}$, for $\theta_{\perp} > 10 \text{ mas}$, two objects have these probabilities greater than 20%, i.e., J0941-0143 and J1348+4411. When $\theta_{\perp} > 0.1 \text{ mas}$ is considered, all the 15 objects with viable solutions have $P_{\theta,\perp} > 20\%$. In particular, four objects, 4C+32.25, J0941-0143, J1348+4411, and J1614+2817, have $P_{\theta,\perp} > 50\%$ when $\theta_{\perp} > 0.1 \text{ mas}$. Therefore, J1348+4411 would be intriguing object for follow-up observations, in the sense that it has an appreciable probability to show both Doppler-shifted broads emission lines and off-center spatial displacement.

4.3. Truncation of dust torus and dust poorness of the sample objects

Given V_{cr} and V_{dp} for each object, we also calculated the probability P_{df} of an X-shaped radio object to have *initial* recoiling velocity larger than V_{cr} and the probability P_{dp} to have recoiling velocity larger than V_{dp} . The probability P_{df} is also the probability for a sample object to have type transition from radio galaxies to quasars and to become “dust free”.

We did not present the probability P_{df} in Table 1, because it is less than 20% for most of the objects except for the quasar 4C+01.30 and radio galaxy J1348+4411. The probability P_{df} for 4C+01.30 to have recoiling velocity larger than its critical velocity $V_{\text{cr}} \approx 700 \text{ (1000) km s}^{-1}$ is about 50% (30%), assuming $f_{\text{bol}} = 20 \text{ (5)}$. In particular, for $40^\circ < w_1 < 60^\circ$ (so that torus is “edge-on” in the initial configuration) the resulting probability for this object to be dust-free is about 34% (60%). This result implies that the AGN could be obscured before binary black hole merger, but the SMBH may have left behind the entire dust torus due to recoil and now transformed into a quasar. While for J1348+4411, its low critical velocity $V_{\text{cr}} \approx 560 \text{ (800) km s}^{-1}$ suggests that $P_{\text{df}} \simeq 63\% \text{ (45\%)}$, thus the object may transform to a quasar or broad emission line radio galaxy. However, the probability

for the object to remain as a radio galaxy is 37% (55%) and not negligible. Therefore, non-detection of broad emission lines does not imply that the SMBHB spin-flip model is completely excluded for this object.

The probability P_{dp} of an X-shaped radio object to have recoiling velocity larger than V_{dp} and to become “dust poor” is given in Column (14) of Table 1, assuming that $f_{\text{bol}} = 10$ and $f_{\text{tor}} = 20$. The upper and lower indices show the upper and lower limits to P_{dp} when a range of bolometric correction factor $5 < f_{\text{bol}} < 20$ and torus size factor $10 < f_{\text{tor}} < 40$ are considered. Among the 15 objects with valid solutions, 12 have $P_{\text{dp}} > 50\%$, and six of them even have $P_{\text{dp}} \gtrsim 80\%$. The upper limit of P_{dp} is greater than 70% for almost all objects, and even greater than 95% for 4C+01.30 and J1348+4411. The poorness of dust in AGN can be observationally tested with the aid of IR satellites such as *Spitzer* (Jiang et al. 2010; Hao et al. 2010; Hal et al. 2011). Therefore, the six objects with $P_{\text{dp}} \gtrsim 80\%$, namely, 3C192, 4C+32.25, J0941-0143, 4C+01.30, J1207+3352, and J1348+4411, would be interesting targets for IR follow-up observations. We note that for 3C192, 4C+32.25, and J1207+3352, the probabilities for the off-center displacement L_{\perp} to be smaller than the typical size of dust torus are $> 90\%$. The SMBHs in these objects are likely settling back in the galaxy nuclei and may become obscured by a new-forming, next-generation dust torus.

4.4. Comments on individual objects

Figures 6-8 show the cumulative distribution functions of the LOS velocity V_{\parallel} and of the apparent spatial off-center displacement L_{\perp} in host galaxies for the 15 objects in our sample which have numerical solutions fulfilling observational constraints. Here we give detailed comments for the objects one by one.

J0001-0033: a radio galaxy at $z=0.247$ (Figure 6). The probability of having Doppler-shifted broad emission lines with $V_{\parallel} > 200 \text{ km s}^{-1}$ is $< 1.5\%$, consistent with 0 given the uncertainties in our model assumptions. The probability of having AGN off-center displacement with $\theta_{\perp} > 0.1 \text{ mas}$ is about 40%. The critical velocity V_{dp} ranges from 450 to 1300 km s^{-1} , when the uncertainties in f_{bol} and f_{tor} are considered. The corresponding probability of being “dust-poor” ranges from 76% to 12%. The critical velocity V_{cr} ranges from 2800 to 4000 km s^{-1} , resulting in a negligible probability of being “dust-free”.

J0049+0059: a radio galaxy at $z=0.304$ (Figure 6). The probabilities of detecting Doppler-shifted broad emission lines with $V_{\parallel} > 200 \text{ km s}^{-1}$ and AGN off-center displacement with $\theta_{\perp} > 10 \text{ mas}$ are consistent with 0. The probability of having AGN off-center dis-

placement with $\theta_{\perp} > 0.1$ mas is about $40 \sim 50\%$. The critical velocity V_{dp} ranges from 560 to 1600 km s^{-1} , when the uncertainties in f_{bol} and f_{tor} are considered. The corresponding probability of being “dust-poor” ranges from 64% to $(1 \sim 2)\%$. The critical velocity V_{cr} ranges from 3600 to 5100 km s^{-1} , resulting in a negligible probability of being “dust-free”.

J0808+2409 (3C192): a radio galaxy at $z=0.060$ (Figure 6). Notice that the distribution functions of V_{\parallel} and θ_{\perp} vary with w_1 by as large as an order of magnitude. The probability of having Doppler-shifted broad lines with $V_{\parallel} > 200 \text{ km s}^{-1}$ is non-zero, but $< 5\%$. The probability of having AGN off-center displacement with $\theta_{\perp} > 0.1$ mas is about 50%. The critical velocity V_{dp} ranges from 240 to 690 km s^{-1} , when the uncertainties in f_{bol} and f_{tor} are considered. The corresponding probability of being “dust-poor” ranges from approximately 56% to 89%. The critical velocity V_{cr} ranges from 1500 to 2200 km s^{-1} , resulting in a negligible probability of being “dust-free”.

J0831+3219 (4C+32.25): a radio galaxy at $z=0.051$ (Figure 6). For $60^{\circ} < w_1 \leq 90^{\circ}$, none of the 10^8 trial Monte Carlo simulations produces a solution fulfilling all the observational constraints. While for other w_1 , the probabilities of detecting Doppler-shifted broad emission lines with $V_{\parallel} > 200 \text{ km s}^{-1}$ and AGN off-center displacement with $\theta_{\perp} > 10$ mas are consistent with 0. The probability of having AGN off-center displacement with $\theta_{\perp} > 0.1$ mas is about 50~63%. The critical velocity V_{dp} ranges from 200 to 550 km s^{-1} , when the uncertainties in f_{bol} and f_{tor} are considered. The corresponding probability of being “dust-poor” ranges from approximately 66% to 87%. The critical velocity V_{cr} ranges from 2000 to 5500 km s^{-1} , resulting in a negligible probability of being “dust-free”.

J0859-0433: a radio galaxy at $z=0.356$ (Figure 6). The probability of $V_{\parallel} > 200 \text{ km s}^{-1}$ is $< 8\%$. The probabilities of have AGN off-center displacement with $\theta_{\perp} > 10$ mas is $< 6\%$, while the probability for $\theta_{\perp} > 0.1$ mas ranges from 46% to 60%. We do not have data about the bolometric luminosity for this object thus cannot give an estimation to the probability of being “dust-poor” or “dust-free”.

J0924+4233: a radio galaxy at $z=0.227$ (Figure 6). For $60^{\circ} < w_1 \leq 90^{\circ}$, none of the 10^8 trial Monte Carlo simulations gives a solution fulfilling all the observational constraints. While for other w_1 , the probability of having Doppler-shifted broad emission lines with $V_{\parallel} > 200 \text{ km s}^{-1}$ is consistent with 0, given the uncertainties in our model assumptions. The probability of having AGN off-center displacement with $\theta_{\perp} > 10$ mas is non-zero, but $< 8\%$, while the probability for $\theta_{\perp} > 0.1$ mas ranges from 41% to 54%. The critical velocity V_{dp} ranges from 350 to 980 km s^{-1} , when the uncertainties in f_{bol} and f_{tor} are considered. The corresponding probability of being “dust-poor” ranges from

approximately 30% to 83%. The critical velocity V_{cr} ranges from 2200 to 3100 km s⁻¹, resulting in a negligible probability of being “dust-free”.

J0941-0143: a radio galaxy at $z=0.384$ (Figure 7). The probability of having Doppler-shifted broad emission lines with $V_{\parallel} > 200$ km s⁻¹ is $< 15\%$. The probabilities of having AGN off-center displacement with $\theta_{\perp} > 10$ mas is about 30% and the probability for $\theta_{\perp} > 0.1$ mas is about 57%. The critical velocity V_{dp} ranges from 190 to 550 km s⁻¹, when the uncertainties in f_{bol} and f_{tor} are considered. The corresponding probability of being “dust-poor” ranges from approximately 67% to 91%. The critical velocity V_{cr} ranges from 1200 to 1700 km s⁻¹, and the resulting probability of being “dust-free” is $0 \sim 17\%$.

J0941+3944 (3C223.1): a radio galaxy at $z=0.107$ (Figure 7). For $60^{\circ} < w_1 \leq 90^{\circ}$, none of the 10^8 trial Monte Carlo simulations gives a solution fulfilling all the observational constraints. While for other w_1 , the probabilities of having Doppler-shifted broad lines with $V_{\parallel} > 200$ km s⁻¹ and AGN off-center displacement with $\theta_{\perp} > 10$ mas are both consistent with $< 8\%$, given the uncertainties in our model assumptions. For $\theta_{\perp} > 0.1$ mas, the probability is about 24%. The critical velocity V_{dp} ranges from 200 to 580 km s⁻¹, when the uncertainties in f_{bol} and f_{tor} are considered. The corresponding probability of being “dust-poor” ranges from 54% to 89%. The critical velocity V_{cr} ranges from 2000 to 5800 km s⁻¹. The resulting probability of being “dust-free” is $(0.01 \sim 4.4)\%$ for $20^{\circ} < w_1 < 40^{\circ}$ and $(0.08 \sim 12)\%$ for $40^{\circ} < w_1 < 60^{\circ}$.

J1005+1154: a radio galaxy at $z=0.166$ (Figure 7). For $60^{\circ} < w_1 \leq 90^{\circ}$, none of the 10^8 trial Monte Carlo simulations produces a solution satisfying all the observational constraints. While for other w_1 , the probabilities of showing Doppler-shifted broad emission lines with $V_{\parallel} > 200$ km s⁻¹ and AGN off-center displacement with $\theta_{\perp} > 10$ mas are consistent with 0, given the uncertainties in our model assumptions. For $\theta_{\perp} > 0.1$ mas, the probability ranges from 23% to 42%. The critical velocity V_{dp} ranges from 350 to 1000 km s⁻¹, when the uncertainties in f_{bol} and f_{tor} are considered. The corresponding probability of being “dust-poor” ranges from 25% to 76%. The critical velocity V_{cr} ranges from 2200 to 3200 km s⁻¹, resulting in a negligible probability of being “dust-free”.

J1020+4831 (4C+48.29): a radio galaxy at $z=0.053$ (Figure 7). The probability of detecting Doppler-shifted broad emission lines with $V_{\parallel} > 200$ km s⁻¹ is consistent with 0, given the uncertainties in our model assumptions. The probability of detecting AGN off-center displacement with $\theta_{\perp} > 10$ mas is non-zero, but $< 7\%$. For $\theta_{\perp} > 0.1$ mas, the probability is about 45%. The critical velocity V_{dp} ranges from 220 to 620 km s⁻¹, when the uncertainties in f_{bol} and f_{tor} are considered. The corresponding probability of being “dust-poor” ranges from 58% to 87%. The critical velocity V_{cr} ranges from

1400 to 2200 km s⁻¹. The resulting probability of being “dust-free” is (0 ~ 11)% for 20° < w_1 < 40°, (0 ~ 7.9)% for 40° < w_1 < 60°, and (0 ~ 8.2)% for 60° < w_1 < 90°.

J1130+0058 (4C+01.30): a radio quasar at $z=0.132$ (Figure 7). For 60° < w_1 ≤ 90°, none of the 10⁸ trial Monte Carlo simulations produces a solution satisfying all the observational constraints. While for other w_1 , the probability of $V_{\parallel} > 500$ km s⁻¹ is < 11%, but the probability of $V_{\parallel} > 200$ km s⁻¹ ranges from 15% to 20%. The probability of detecting AGN off-center displacement is non-zero, ranging from (16 ~ 24)% in the case 20° < w_1 < 40° to (25 ~ 33)% in the case 40° < w_1 < 60°. The critical velocity V_{dp} ranges from 700 to 990 km s⁻¹, when the uncertainties in f_{bol} and f_{tor} are considered. The corresponding probability of being “dust-poor” ranges from 80% to 96%. The critical velocity V_{cr} ranges from 1100 to 3100 km s⁻¹. The resulting probability of being “dust-free” is (25 ~ 50)% for 20° < w_1 < 40° and (34 ~ 59)% for 40° < w_1 < 60°. It is interesting to note that Wang et al. (2003) reported a possible large offset, 3.5 ″, in this object between the radio core and the photometric center of the host galaxy. Our Monte Carlo simulations suggest that the observation would require a recoiling velocity of $V > 4000$ km s⁻¹ at a confidence level of 99.9%. Such high recoiling velocity is extremely difficult to achieve by asymmetric gravitational wave radiation of circular SMBHB orbit. This implies that either the two SMBHs merge along hyperbolic orbit (Healy et al. 2009) or a mechanism other than recoiling SMBH is needed to produce the large displacement.

J1140+1057: a radio galaxy at $z=0.081$ (Figure 8). The probability of having Doppler-shifted broad emission lines with $V_{\parallel} > 200$ km s⁻¹ is generally < 8%. The probability of having AGN off-center displacement with $\theta_{\perp} > 10$ mas is about 18%, increasing to about 50% for $\theta_{\perp} > 0.1$ mas. The critical velocity V_{dp} ranges from 250 to 700 km s⁻¹, when the uncertainties in f_{bol} and f_{tor} are considered. The corresponding probability of being “dust-poor” ranges from 55% to 87%. The critical velocity V_{cr} ranges from 1600 to 2200 km s⁻¹, resulting in a negligible probability of being “dust-free”.

J1207+3352: a radio galaxy at $z=0.079$ (Figure 8). For 60° < w_1 ≤ 90°, none of the 10⁸ trial Monte Carlo simulations produces a solution satisfying all the observational constraints. While for other w_1 , the probabilities of showing Doppler-shifted broad emission lines with $V_{\parallel} > 200$ km s⁻¹ and AGN off-center displacement with $\theta_{\perp} > 10$ mas are both ≤ 15%. For $\theta_{\perp} > 0.1$ mas, the probability is about 43%. The critical velocity V_{dp} ranges from 160 to 440 km s⁻¹, when the uncertainties in f_{bol} and f_{tor} are considered. The corresponding probability of being “dust-poor” ranges from approximately 67% to 92%. The critical velocity V_{cr} ranges from 980 to 1400 km s⁻¹. The resulting probability of being “dust-free” is (2.7 ~ 17)% for 20° < w_1 < 40° and

(8.6 ~ 32)% for $40^\circ < w_1 < 60^\circ$.

J1348+4411: a radio galaxy at $z=0.267$ (Figure 8). The probability of $V_{\parallel} > 500 \text{ km s}^{-1}$ is about 13%, but the probability of $V_{\parallel} > 200 \text{ km s}^{-1}$ increases steeply to about 35%. The probability of having AGN off-center displacement is ranging from about 52% in the case of $\theta_{\perp} > 10 \text{ mas}$ to about 63% in the case of $\theta_{\perp} > 0.1 \text{ mas}$. The critical velocity V_{dp} ranges from 89 to 250 km s^{-1} , when the uncertainties in f_{bol} and f_{tor} are considered. The corresponding probability of being “dust-poor” ranges from 85% to 97%. The critical velocity V_{cr} ranges from 560 to 800 km s^{-1} . For all w_1 , the probability of being “dust-free” and become type I AGN is (45 ~ 64)%. The lack of broad line in this object implies that $V < V_{\text{cr}}$. If $V < V_{\text{cr}}$ is required, our Monte Carlo simulations suggests that $P(V_{\parallel} > 200 \text{ km s}^{-1})$ and $P(\theta_{\perp} > 0.1 \text{ mas})$ both decrease to $< 10\%$, but P_{dp} is still in the range (70 ~ 90)%. Alternatively, it is possible that this radio galaxy intrinsically lacks broad emission lines like in some AGNs and quasars (e.g. Fan et al. 1999).

J1614+2817: a radio galaxy at $z=0.108$ (Figure 8). The probabilities of having Doppler-shifted broad emission lines with $V_{\parallel} > 200 \text{ km s}^{-1}$ and AGN off-center displacement with $\theta_{\perp} > 10 \text{ mas}$ are non-zero, but $< 20\%$. For $\theta_{\perp} > 0.1 \text{ mas}$, the probability increases to about 65%. The critical velocity V_{dp} ranges from 610 to 1700 km s^{-1} , when the uncertainties in f_{bol} and f_{tor} are considered. The corresponding probability of being “dust-poor” ranges from nearly 0% to 65%. The critical velocity V_{cr} ranges from 3800 to 5400 km s^{-1} , resulting in a negligible probability of being “dust-free”.

5. Discussions and conclusions

A popular model in the literature suggested that the X-shaped radio sources form because of jet reorientation following the spin flip of SMBHs at SMBHB mergers. Numerical relativity suggested that the black hole merger not only leads to a spin flip but also to a gravitational kick of the post-merger black holes. In this paper, we investigated with Monte Carlo simulations the distribution function of the spin-flip angles and recoiling velocities of the post-merger SMBHs, and the detectability of recoiling SMBHs, in the forms of Doppler-shifted spectral lines and off-center AGNs, in radio sources showing spin-flip signatures of jet reorientation. We also collected a sample of 19 X-shaped radio objects and calculated for all the sample objects the spectral kinematic offsets V_{\parallel} , the apparent spatial off-center displacements L_{\perp} , and the degree of dust-torus truncation because of the gravitational kick.

Because the spin flip and recoiling velocity strongly depend on the parameters q , \mathbf{a}_1 , \mathbf{a}_2 ,

and \mathbf{e}_s of SMBHB system, we first investigated the distribution of mass ratio q in spin-flip radio sources with given apparent jet reorientation angles, assuming that the spin parameter a of jet-ejecting SMBHs has $a \geq 0.9$. Our results indicate that to cause significant apparent jet reorientation the mass ratio cannot be smaller than a minimum value $q_{\min} \sim 0.1$. The larger the apparent jet reorientation angle is, the larger the minimum mass ratio will be. For spin-flip radio sources with apparent jet reorientation angle $15^\circ < \delta < 40^\circ$, $q_{\min} \sim 0.05$ and the most probable mass ratio is $q \simeq 0.3$, while for spin-flip radio sources with $65^\circ < \delta < 90^\circ$, $q_{\min} \simeq 0.15$ and the most probable mass ratio is $q \gtrsim 0.6$. Our results suggest that if an observed jet reorientation is indeed due to the spin flip following a SMBHB merger, the merger must be major merger with $q \gtrsim 0.2-0.3$. If the spin-flip model for radio sources of jet reorientation could be confirmed, our results suggest that we can measure the distribution of SMBHB mass ratio in luminous radio sources and give statistic constraints on the hierarchical galaxy formation model and the growth history of SMBHs.

Having the mass ratio distribution, we investigated the distributions of spin flip angle and recoiling velocity in spin-flip radio sources. Our results showed that the larger the SMBHB mass ratio is, the larger the the most possible spin flip angle and the recoiling velocity will be. For typical major merger mass ratio $q = 0.3$, $q = 0.7$ and $q = 1.0$, the most possible spin flip angles are moderate and increase with mass ratio from $\Delta = 19^\circ$ for $q = 0.3$, and 25° for $q = 0.7$ to 30° for $q = 1$. The spin flip angle is hardly ever larger than $\Delta \sim 55^\circ$. Our results imply that any apparent jet reorientation angle $\delta \gtrsim 60^\circ$ is due to projection effect. For $q = 0.3$, the recoiling velocity ranges from about zero to larger than 1200 km s^{-1} with a most possible velocity $V \sim 600 \text{ km s}^{-1}$. While for $q \gtrsim 0.7$, the distribution of recoiling velocity is similar and ranges from about 0 to larger than 2100 km s^{-1} with most probable velocity $\hat{V} \sim 900 \text{ km s}^{-1}$. For major mergers with $q \gtrsim 0.3$, almost all recoiling SMBHs move nearly along the final jet orientation within a angle of 40° . Alignment of spin axes with orbital angular momentum of SMBHB prior to the black hole coalescence would significantly reduce the recoiling velocity and spin-flip angle, but tighten the correlation between the orientations of final spin and recoiling velocity. Our results suggest that to efficiently detect recoiling SMHBs with Doppler shifted spectral broad emission lines, one should preferentially observe nearly face-on AGNs, e.g. radio loud quasars or blazars among which the broad emission lines are nearly maximumly Doppler-shifted for a given recoiling velocity. This conclusion is also consistent with present observations in the literature that all candidates for recoiling SMBHs are bright quasars and the measured Doppler-shifting recoiling velocity is preferentially very larger (e.g. Komossa et al. 2008). However, to detect recoiling SMBHs in radio galaxies, one should try to measure the apparent spatial off-center displacements of AGNs relative to the centers of the host galaxies because the recoiling SMBHs are moving nearly along the jet axes, which are at large angles with respect to LOS.

Even in some quasars, recoiling SMBHs may be discovered by measuring the apparent spatial off-center displacements because some radio galaxies and Type II quasars may transit to Type I quasars due to the recoiling oscillations as suggested by Komossa & Merritt (2008a). For minor mergers with $q \sim 0.1$, both the spin-flip angle and the recoiling velocity narrowly distribute with peaks at the most possible angle $\Delta \sim 12^\circ$ and velocity $V \sim 150 \text{ km s}^{-1}$.

In order to use the observed jet reorientation angles in spin-flip radio sources to constrain the observable spectral kinematic offsets V_{\parallel} and apparent spatial off-center displacements L_{\perp} , we projected the spin-flip angles and the recoiling velocities along and vertical to LOS and investigated their correlations. An analytical 1-D model is used to calculate the deceleration of a recoiling SMBH due to dynamical friction, and the elapsed time since the black hole gets kicked is estimated from the size of the radio morphology. In general, V_{\parallel} in spin-flip radio sources is smaller than 2000 km s^{-1} and L_{\perp} hardly ever exceeds 2 kpc. However, we should note that the conclusion is valid only for quasars with SMBHBs of circular orbits. For two SMBHBs merging along hyperbolic orbits, it is possible to have a recoiling velocity significantly larger than 2000 km s^{-1} (Healy et al. 2009). Our results indicate that in radio sources showing spin-flip signatures of jet reorientation, detectable Doppler-shifted broad emission lines are mainly contributed by GPS and CSS sources with large apparent spin-flip angles. The detection rate of Doppler-shifted broad emission lines in a sample of GPSs/CSSs with $\delta > 40^\circ$ could be as high 50%. For GRSs, deceleration due to dynamical friction has significantly reduced V_{\parallel} , so the probability of detecting Doppler-shifted broad emission lines is typically $\lesssim 10\%$. Detecting AGN off-center displacement requires astrometric observations with high angular resolution. For current telescopes with limit resolution up to 10 mas, detection of off-center displacement would be limited to the GPS/CSS sources within a distance of 100 Mpc. However, future interferometer missions with sub-mas resolution or higher, such as Gaia, would allow detection of off-center AGNs in GPS, CSS, and GRSs at a much larger distance. Our results suggest that to efficiently detect the recoiling SMBHBs in spin-flip radio sources, one should select a sample of GPS/CSS sources with apparent jet reorientation angles $\delta \gtrsim 40^\circ$.

When the SMBH in an AGNs gets kicked, the outer part of the dust torus in AGN unification model may become unbound and the dust torus is truncated, leading to the transition of the AGN from dust rich to “dust poor” or even to “dust free”. When a FR II radio galaxy or an obscured quasar becomes “dust free”, it should transform to an unobscured broad emission line quasar. We calculated the minimum recoiling velocities for partial or full truncation of dust torus and estimated their detectability in typical spin-flip radio sources with different apparent jet reorientation angles δ . Our results suggest that about 11% spin-flip radio galaxies with $\delta \gtrsim 40^\circ$ and about 1% with $\delta \lesssim 40^\circ$ will become “dust free” and broad emission line AGNs, if broad line regions are present. Our results imply that

quasars with larger bolometric luminosity and smaller black hole mass should have higher probability to become “dust free”. The velocity for dust torus to be partially truncated is typically lower than the most-probable recoiling velocity, therefore most X-shaped radio sources should be “dust poor”. Quasars may become weak emission line objects, if the broad emission regions are partially truncated due to gravitational recoiling. This is possible for a quasar with small black hole mass ($\sim 10^6 M_\odot$) radiating at the Eddington limit. We note that without gas replenishing the accretion disks, the dust-free and weak-line quasars formed by recoiling SMBHs are relatively short-living ($\lesssim 1$ Myr), because the combination of high recoiling velocity ($\gtrsim 10^3$ km s $^{-1}$), small black hole mass ($\lesssim 10^7 M_\odot$), and large bolometric luminosity ($\gtrsim 10^{45}$ erg s $^{-1}$) will significantly reduce the lifetimes of the accretion disks around the recoiling black holes (e.g. Loeb 2007). This argument implies that among X-shaped radio sources whose host galaxies are typically gas-poor elliptical, the ones with long active jets ($\gtrsim 100$ kpc or $t_a \gtrsim 3 \times 10^6$ yr for a typical advancing speed $0.1c$ of hot spot in FRII radio galaxies) and small black hole masses ($\lesssim 10^7 M_\odot$) are unlikely to host dust-free and weak-line quasars.

We then selected a sample of 19 X-shaped radio objects, consisting of 18 X-shaped radio galaxies and 1 quasar, and for each sample object we calculated the distribution functions of the LOS recoiling velocity V_\parallel and the apparent spatial off-center displacement L_\perp , as well as the critical recoiling velocities V_{cr} and V_{dp} for partial and complete truncation of dust torus. To do the calculations, we measured the apparent jet reorientation angles from the radio images and collected the central SMBH masses, the optical luminosities of AGNs, the viewing angles and dynamic ages of the active lobes from the literature. Our results showed that most X-shaped radio objects in the sample have negligible V_\parallel ($P_{v,\parallel} < 10\%$), except for J0941-0143, 4C+01.30, J1348+4411, and J1614+2817. All the 15 sample objects with valid Monte Carlo solutions have significant probabilities ($> 20\%$) to show AGN off-center displacements when a spatial resolution of 0.1 mas is considered. In particular, the radio galaxy J1348+4411 have appreciable probability to show both Doppler-shifted broad emission lines ($P_{v,\parallel} \simeq 40\%$) and off-center spatial displacement ($P_{\theta,\perp} \simeq 55\%$), therefore would be intriguing target for follow-up observations. Our results also showed that the sample X-shaped radio objects have high probabilities to be “dust-poor”. The probabilities for X-shaped radio galaxy J1348+4411 and quasar 4C+01.30 are always higher than 80%, despite the uncertainties in torus size and bolometric correction factor. Because of the high probability of being both dust-poor and offset from galaxy center, these two objects would be interesting targets for IR follow-up observations to test the dust-poorness. Besides, J1348+4411 and 4C+01.30 also have the highest probability in our sample to be “dust-free” and non-obscured. The fact that 4C+01.30 is already a quasar implies that this object could be an obscured AGN before binary black hole merger, but may have transformed into a

quasar after recoil takes place. Detecting the predicted off-center displacement and Doppler shifted broad emission lines would strongly support that 4C+01.30 is a recoiling SMBH. For J1348+4411, the lack of broad line in this object suggests that the recoiling velocity is toward the lower end of the predicted distribution function, but the probability of being dust-poor is still higher than 70%.

The detection of the predicted observational signatures of recoiling SMBHs in X-shaped radio sources would give final confirmation of the spin-flip model for X-shaped radio sources. While, if none of the predicted signatures is detected in X-shaped radio sources, the SMBHB spin-flip model for the formation of X-shaped radio feature would be most likely excluded, unless our assumptions for the initial conditions of SMBHB mergers are severely unrealistic. However, this does not imply that X-shaped radio sources do not harbor SMBHBs at center, because jet reorientation may form due to the interaction of SMBHB and accretion disk (Liu 2004). According to the disk-binary interaction model, the final recoiling velocity of a SMBH is small due to the alignment between the black hole spin axes and the orbital angular momentum before the merger, therefore neither the spectral kinematic offset nor the spatial AGN off-center displacement are as large as those in the spin flip model.

We are grateful to the anonymous referee for valuable comments which help us to significantly improve the quality of this paper. We also thank Luciano Rezzolla, Joan Centrella, Stefanie Komossa, Xuebing Wu, Monica Colpi, Zhiqiang Shen for helpful discussions. This work is supported by the Chinese national 973 program (2007CB815405), the National Natural Science Foundation of China (NSFC11073002), and the China Scholarship Council for financial support (2009601137). DW thanks the support of the Maoyugang Undergraduate Research Fellowship. The numerical computations were carried out on the SGI Altix 330 system at the Astronomy Department, Peking University.

REFERENCES

- Alexander, P., & Leahy, J.P. 1987, MNRAS, 225, 1
- Arav, N., Barlow, T. A., Laor, A., Sargent, W. L. W., & Blandford, R. D. 1998, MNRAS, 297, 990
- Armitage, P. J. & Natarajan, P., 2002, ApJ, 567, L9
- Baker J. G., Boggs, W. D., Centrella J., Kelly B. J., McWilliams S. T., et al. 2008, ApJ, 682, L29

- Baker, J. G., Centrella, J., Choi, D.-I., Koppitz, M., van Meter, J. R., & Miller, M. C. 2006, *ApJ*, 653, L93
- Balashev, S. A., Petitjean, P., Ivanchik, A. V., et al. 2011, *MNRAS*, 418, 357
- Batcheldor, D., Robinson, A., Axon, D. J., Perlman, E. S., & Merritt, D. 2010, *ApJ*, 717, L6
- Begelman M. C., Blandford R. D., Rees M. J., 1980, *Nature*, 287, 307
- Berczik, P., Merritt, D., Spurzem, R., & Bischof, H.-P. 2006, *ApJ*, 642, L21
- Blecha L., Cox T.J., Loeb A., & Hernquist, L. 2011, *MNRAS*, 412, 2154
- Blecha L., & Loeb A., 2008, *MNRAS*, 390, 1311
- Bogdanović, T., Eracleous, M., & Sigurdsson, S., 2009, *ApJ*, 697, 288
- Bonning, E. W., Shields, G. A., & Salvander, S. 2007, *ApJ*, 666, L13
- Boroson, T. A. & Lauer, T. R., 2009, *Nature*, 458, 53
- Campanelli, M., Lousto C. O., Marronetti P., & Zlochower Y., 2006, *Phys. Rev. Lett.*, 96, 111101
- Campanelli, M., Lousto, C.O., Zlochower, Y. & Merritt, D. 2007a, *ApJ*, 659, L5
- Campanelli, M., Lousto, C. O., Zlochower, Y., & Merritt, D. 2007b, *Phys. Rev. Lett.*, 98, 231102
- Capetti, A., Zamfir, S., Rossi, P., Bodo, G., Zanni, C., et al. 2002, *A&A*, 394, 39
- Chatterjee, P., Hernquist, L., & Loeb, A. 2003, *ApJ*, 592, 32
- Chen, X., Liu, F.K., Magorrian, J. 2008, *ApJ*, 676, 54
- Chen, X., Madau, P., Sesana, A., Liu, F.K. 2009, *ApJ*, 697, L149
- Chen, X., Sesana, A., Madau, P., Liu, F.K. 2011, *ApJ*, 729, 13
- Cheung, C.C., 2007, *AJ*, 133, 2097
- Civano, F., et al., 2010, *ApJ*, 717, 209
- Colpi, M., & Dotti, M. 2011, *Adv. Sci. Lett.*, 4, 181 (arXiv:0906.4339)

- Comerford, J., et al., 2009, *ApJ*, 698, 956
- Dennett-Thorpe, J., Scheuer, P. A. G., Laing, R. A., Bridle, A. H., Pooley, G. G., & Reich, W. 2002, *MNRAS*, 330, 609
- Dotti, M., Montuori, C., Decarli, R., Volonteri, M., Colpi, M., & Haardt, F., 2009, *MNRAS*, 398, 73
- Ekers, R.D., Fanti, R., Lari, C., & Parma, P., 1978, *Nature*, 276, 588
- Elitzur, M. 2007, in *ASP Conf. Ser. 373, The Central Engine of Active Galactic Nuclei*, ed. L.C. Ho & J.-M. Wang (San Francisco: ASP), 415
- Eracleous, M., Boroson, T. A., Halpern, J. P., & Liu, J. 2011, *arXiv:1106.2952*
- Fan, X., Strauss, M.A., Gunn, J.E., Lupton, R.H., Carilli, C.L., et al. 1999, *ApJ*, 526, L57
- Fu, H., Myers, A. D., Djorgovski, S. G., & Yan, L. 2010, 733, 103
- Gaskell, C.M. 1996, *ApJ*, 464, L107
- Gonzalez, J.A., Sperhake, U., Bruegmann, B., Hannam, M. D., & Husa, S. 2007, *Phys. Rev. Lett.*, 98, 091101
- Gopal-Krishna, Biermann, P.L., & Wiita, P.J. 2003, *ApJ*, 594, L103
- Gould, A., & Rix, H.-W. 2000, *ApJ*, 532, L29
- Green, P.J., Myers, A.D., Barkhouse, W.A., Mulchaey, J.S., Bennert, V.N., et al. 2010, *ApJ*, 710, 1578
- Gualandris, A., & Merritt, D., 2008, *ApJ*, 678, 780
- Guedes, J., Madau, P., Kuhlen, M., Diemand, J., & Zemp, M. 2009, *ApJ*, 702, 890
- Guedes, J., Madau, P., Mayer, L., & Callegari, S. 2011, *ApJ*, 729, 125
- Hao, H., Elvis, M., Civano, F., & Lawrence, A., 2011, *ApJ*, 733, 108
- Hao, H., Elvis, M., Civano, F., Lanzuisi, G., Brusa, M., et al., 2010, *ApJ*, 724, L59
- Healy, J., Herrmann, F., Hinder, I., Shoemaker, D.M., Laguna, P., & Matzner, R.A. 2009, *Phys. Rev. Lett.*, 102, 041101
- Herrmann, F., Hinder, I., Shoemaker, D., Laguna, P., & Matzner, R. A. 2007, *ApJ*, 661, 430

- Hodges-Kluck, E., Reynolds, C.S., Cheung, C.C., Miller, M.C., 2010, *ApJ*, 710, 1205
- Hughes, S.A. & Blandford, R.D. 2003, *ApJ*, 585, L101
- Jiang, L., Fan, X., Brandt, W.N., Carilli, C.L., Egami, E., et al., 2010, *Nature*, 464, 380
- Jonker, P. G., Torres, M. A. P., Fabian, A. C., Heida, M., Miniutti, G., & Pooley, D. 2010, *MNRAS*, 407, 645
- Kaspi, S., Maoz, D., Netzer, H., Peterson, B.M., Vestergaard, M. & Jannuzi, B.T. 2005, *ApJ*, 629, 61
- Kaspi, S., Smith, P.S., Netzer, H., Maoz, D., Jannuzi, B.T. & Giveon, U. 2000, *ApJ*, 533, 631
- Kauffmann, G. & Haehnelt, M., 2000, *MNRAS*, 311, 576
- Kesden, M., Sperhake, U., & Berti, E. 2010, *ApJ*, 715, 1006
- Komossa, S. 2006, *Mem. Soc. Astron. Italiana*, 77, 733
- Komossa, S. 2010, *IAU Symposium*, 267, 451
- Komossa, S., Burwitz, V., Hasinger, G., Predehl, P., Kaastra, J.S. & Ikebe, Y., 2003, *ApJ*, 582, L15
- Komossa, S. & Merritt, D. 2008b, *ApJ*, 683, L21
- Komossa, S. & Merritt, D. 2008a, *ApJ*, 689, L89
- Komossa, S., Zhou, H., & Lu, H., 2008, *ApJ*, 678, L81
- Kraft, R. P., Hardcastle, M. J., Worrall, D. M., & Murray, S. S., 2005, *ApJ*, 622, 149
- Lal, D.V. & Rao, A.P., 2007, *MNRAS*, 374, 1085
- Landt, H., Cheung, C.C. & Healey, S.E. 2010, *MNRAS*, 408, 1103
- Leahy, J.P. & Parma, P., 1992, in *Extragalactic Radio Sources: From Beams to Jets*, (eds) Roland J., Sol H., Pelletier G., (Cambridge Univ. Press, Cambridge), p. 307
- Leahy, J.P. & Williams, A.G., 1984, *MNRAS*, 210, 929
- Li, S.; Liu, F.K.; Berczik, P.; Chen, X.; & Spurzem, R. 2011, *ApJ*, submitted
- Liu, F. K., 2004, *MNRAS*, 347, 1357

- Liu, F.K. & Chen, X. 2007, ApJ, 671, 1272
- Liu, F.K., Li, S. & Xian, C. 2009, ApJ, 706, L133
- Liu, F. K., Liu, B. F., & Xie, G. Z., 1997, A&AS, 123, 569
- Liu, F. K. & Wu, X. B., 2002, A&A, 388, L48
- Liu, F. K., Wu, X.-B., & Cao, S. L. 2003, MNRAS, 340, 411
- Liu, F. K., Xie, G. Z., & Bai, J. M., 1995, A&A, 295, 1
- Liu, F. K., Zhao, G., & Wu, X. B., 2006, ApJ, 650, 749
- Liu, X., Greene, J. E., Shen, Y., & Strauss, M. A. 2010a, ApJ, 715, L30
- Liu, X., Shen, Y., Strauss, M. A., Greene, J. E., 2010b, ApJ, 708, 427
- Loeb, A. 2007, Phys. Rev. Lett., 99, 041103
- Lousto, C. O., Campanelli, M., Zlochower, Y., & Nakano, H. 2010a, Classical and Quantum Gravity, 27, 114006
- Lousto, C. O., Nakano, H., Zlochower, Y., & Campanelli, M. 2010b, Phys. Rev. D, 81, 084023
- Lousto, C. O., & Zlochower, Y. 2008, Phys. Rev. D, 77, 044028
- Lu, J.R., Ghez, A.M., Yelda, S., Do, T., Clarkson, W., et al. 2010, Proc. SPIE, Vol.7736, 51
- Madau, P. & Quataert, E. 2004, ApJ, 606, L17
- Magain P., Letawe G., Courbin F., Jablonka Pl., Jahnke K., Meylan G., & Wisotzki G., 2005, Nature, 437, 381
- Merritt, D., 2006, ApJ, 648, 976
- Merritt, D., & Ekers, R. D. 2002, Science, 297, 1310
- Merritt, D. & Milosavljević, M., 2005, Liv. Rev. Rel., 8, 8
- Merritt, D., Milosavljevic, M., Favata, M., Hughes, S. A. & Holz, D.E., 2004, ApJ, 607, L9
- Mezcua, M., Lobanov, A.P., Chavushyan, V.H. & Leon-Tavares, J. 2011, A&A, 527, A38
- Nenkova, M., Sirocky, M.M., Nikutta, R., Ivezić, Z. & Elitzur, M. 2008, ApJ, 685, 160
- O’Dea, C. P. 1998, PASP, 110, 493

- Owsianik I., Conway J. E., Polatidis A. G., 1999, *New Astron. Rev.*, 43, 669
- Popovic, L. C., Jovanovic, P., Stalevski, M., et al. 2011, arXiv:1109.3659
- Pretorius F. 2005, *Phys. Rev. Lett.*, 95, 121101
- Rezzolla, L., Barausse, E., Dorband, E. N., Pollney, D., Reisswig, C., et al. 2008, *Phys. Rev. D*, 78, 044002
- Robinson, A., Young, S., Axon, D. J., Kharb, P., & Smith, J. E. 2010, *ApJ*, 717, L122
- Rodriguez, C., Taylor, G. B., Zavala, R. T., Peck, A. B., Pollack, L.K., & Romani, R.W. 2006, *ApJ*, 646, 49
- Rosario, D. J., McGurk, R. C., Max, C. E., Shields, G. A., & Smith, K. L. 2011, *ApJ*, 739, 44
- Saripalli, L. & Subrahmanyam, R., 2009, *ApJ*, 695, 156
- Schoenmakers, A.P., de Bruyn, A.G., Röttgering, H.J.A., van der Laan, H., & Kaiser, C.R. 2000, *MNRAS*, 315, 371
- Sesana, A., Haardt, F., & Madau, P. 2008, *ApJ*, 686, 432
- Shen, Y., Liu, X., Greene, J. E., & Strauss, M. A. 2011, *ApJ*, 735, 48
- Shields, G. A., et al., 2009, *ApJ*, 707, 936
- Sillanpaa, A., Haarala, S., Valtonen, M.J., Sundelius, B. & Byrd, G.G. 1988, *ApJ*, 325, 628
- Smith, K. L., Shields, G. A., Bonning, E. W., McMullen, C. C., & Salviander, S., 2010, *ApJ*, 716, 866
- Springel, V., White, S.D.M., Jenkins, A., Frenk, C.S., Yoshida, N., et al. 2005, *Nature*, 435, 629
- Stockton, A. & Farnham, T., 1991, *ApJ*, 371, 525
- Tanaka, T. & Haiman, Z. 2009, *ApJ*, 696, 1798
- Terzić, B., & Graham, A. W., 2005, *MNRAS*, 362, 197
- Tsalmantza, P., Decarli, R., Dotti, M., & Hogg, D. W. 2011, arXiv:1106.1180
- Urry, C. M., & Padovani, P. 1995, *PASP*, 107, 803

- van Meter, J.R., Miller, M.C., Baker, J.G., Boggs, W.D. & Kelly, B.J. 2010, ApJ, 719, 1427
- Valtaoja, E., Terasranta, H., Tornikoski, M., Sillanpaa, A., Aller, M.F., et al. 2000, ApJ, 531, 744
- Volonteri, M. 2007, ApJ, 663, L5
- Volonteri, M., Haardt, F., & Madau, P., 2007, ApJ, 582, 559
- Wang, J.-M., Chen, Y.-M., Hu, C., Mao, W.-M., Zhang, S. & Bian, W.-H. 2009, ApJ, 705, L76
- Wang, T.-G., Zhou, H.-Y. & Dong, X.-B. 2003, AJ, 126, 113
- Wirth, A., Smarr, L., & Gallagher, J. S. 1982, AJ, 87, 60
- Wizinowich, P., Acton, D.S., Shelton, C., Stomski, P., Gathright, J., et al. 2000, PASP, 112, 315
- Worrall, D.M., Birkinshaw, M. & Cameron, R.A. 1995, ApJ, 449, 93
- Xu, D. & Komossa, S. 2009, ApJ, 705, L20
- Yu, Q. 2002, MNRAS, 331, 935
- Zhou, H., Wang, T., Zhang, X., Dong, X. & Li, C. 2004, ApJ, 604, L33
- Zier, C., 2005, MNRAS, 364, 583

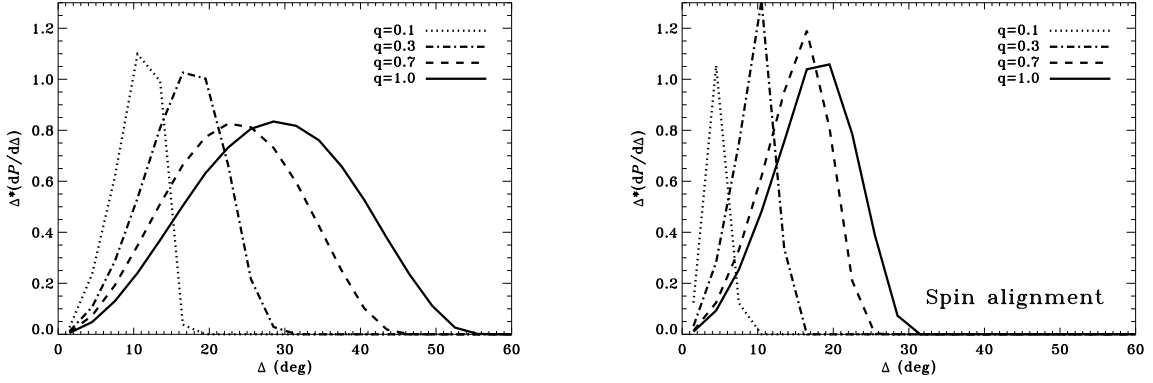


Fig. 2.— Distribution functions of intrinsic spin flip angle Δ for different SMBHB mass ratios, assuming random initial spin orientation (left panel) or initial spin alignment within 30° relative to the binary orbital angular momentum (right panel). Spin-flip angles in the mergers with larger mass ratio generally have broader distributions and the equal-mass mergers give the largest possible spin flip angle. When the initial spin orientations are random (aligned), typical spin flip angles are $\Delta \sim 30^\circ$ ($\sim 19^\circ$) for $q = 1$, $\Delta \sim 25^\circ$ ($\sim 17^\circ$) for $q = 0.7$, and $\Delta \sim 19^\circ$ ($\sim 11^\circ$) for $q = 0.3$. While for minor mergers of $q = 0.1$, the spin flip angles narrowly distribute with $\text{FWHM}(\Delta) \simeq 7^\circ$ ($\simeq 3^\circ$) and a peak at $\Delta = 12^\circ$ ($\sim 4^\circ$).

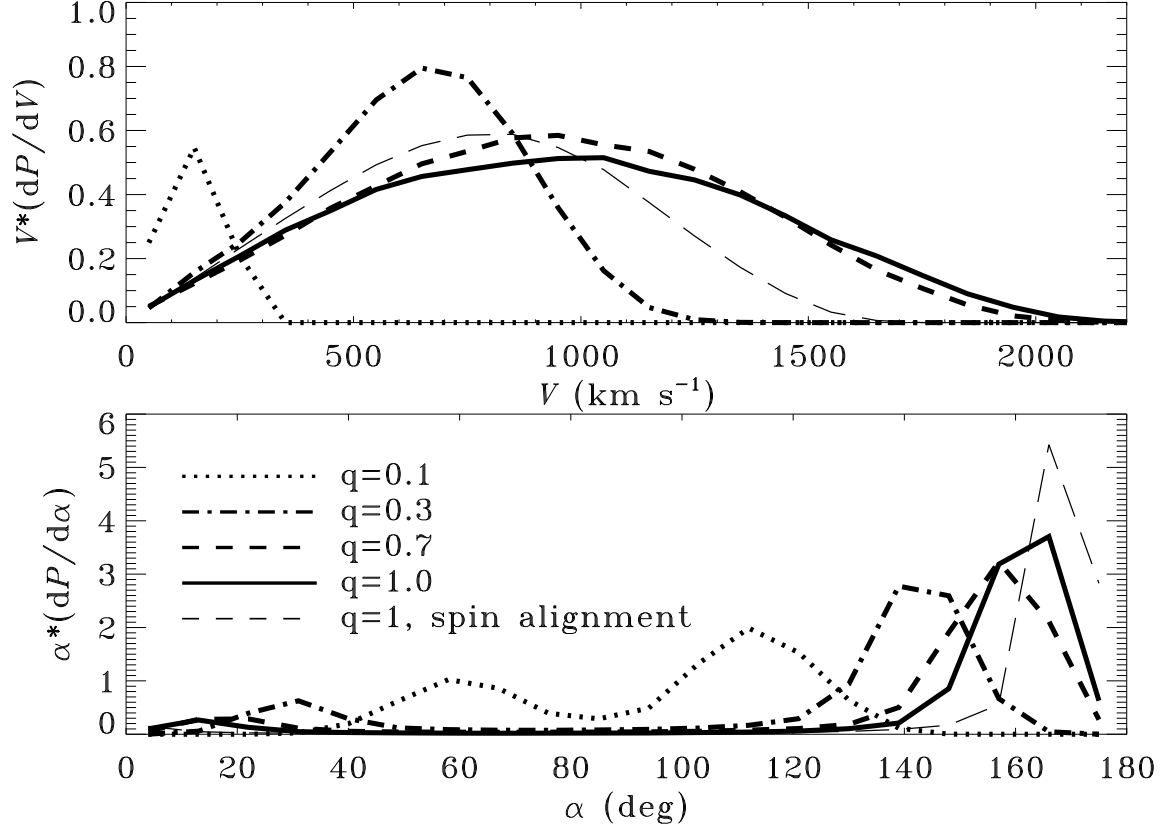


Fig. 3.— (*Upper*) Distribution functions of recoiling velocity V for different black hole mass ratios. For major mergers with $q \gtrsim 0.7$, the distributions of recoiling velocity are almost identical, ranging from 0 to about 2100 km s^{-1} with most possible recoiling velocity $V \sim 900 \text{ km s}^{-1}$. For smaller mass ratios, V distributes in narrower ranges and the fraction with large recoiling velocity decreases rapidly. Most mergers have recoiling velocity $V \sim 600 \text{ km s}^{-1}$ for $q=0.3$. For minor mergers $q \sim 0.1$, recoiling velocity is narrowly peaked at $V \sim 150 \text{ km s}^{-1}$. (*Lower*) Distribution functions of the direction angle α of recoiling velocity relative to the spin axis of post-merger black hole for different mass ratios q . For major mergers of $q \gtrsim 0.3$, recoiling SMBHs move preferentially along the spin axis of post-merger SMBHs within an angle of 40° . For major mergers $q \gtrsim 0.7$, most recoiling SMBHs moves in a direction of $\alpha \gtrsim 165^\circ$. The thin dashed lines in both panels show the results when partial spin alignment is considered.

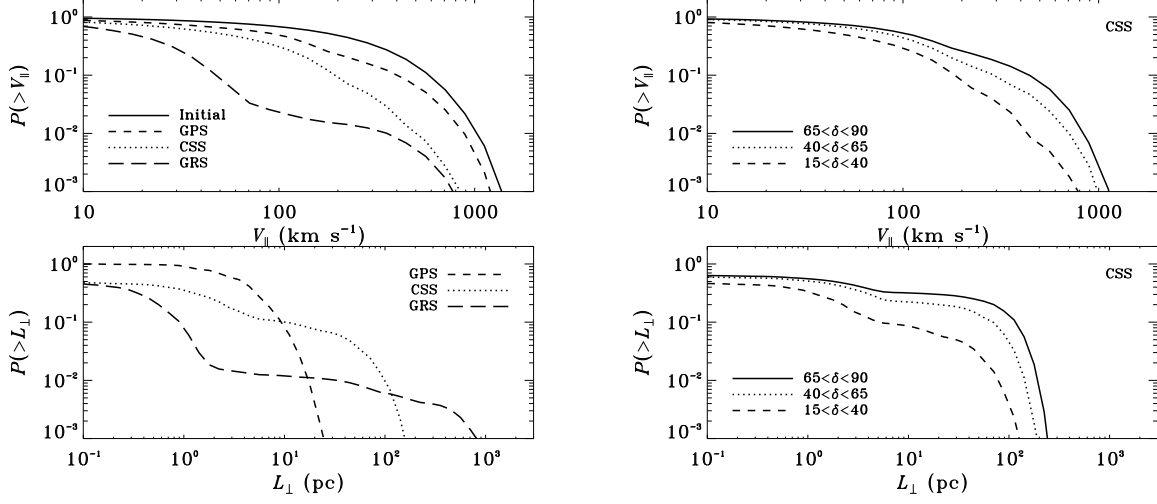


Fig. 4.— Cumulative distribution functions of LOS velocity (*Upper*) and apparent off-center displacement (*Lower*), for spin-flip quasars at initial kick (with quenched jet formation) and with increasing active jet sizes and ages from GPSs to CSSs and finally GRSs (*left*) and for CSS quasars with different apparent spin-flip angles (*right*). The fiducial black hole mass is $10^8 M_{\odot}$ and the stellar velocity dispersion of host galaxy is 200 km s^{-1} .

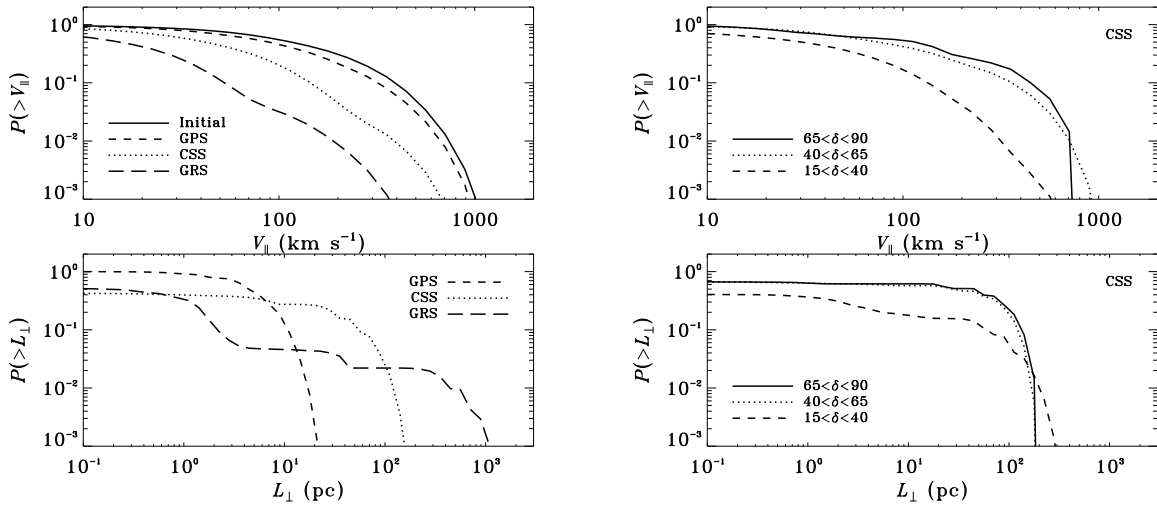


Fig. 5.— The same as Figure 4 but for spin-flip radio galaxies, which have $44.4^{\circ} < w_2 < 90^{\circ}$.

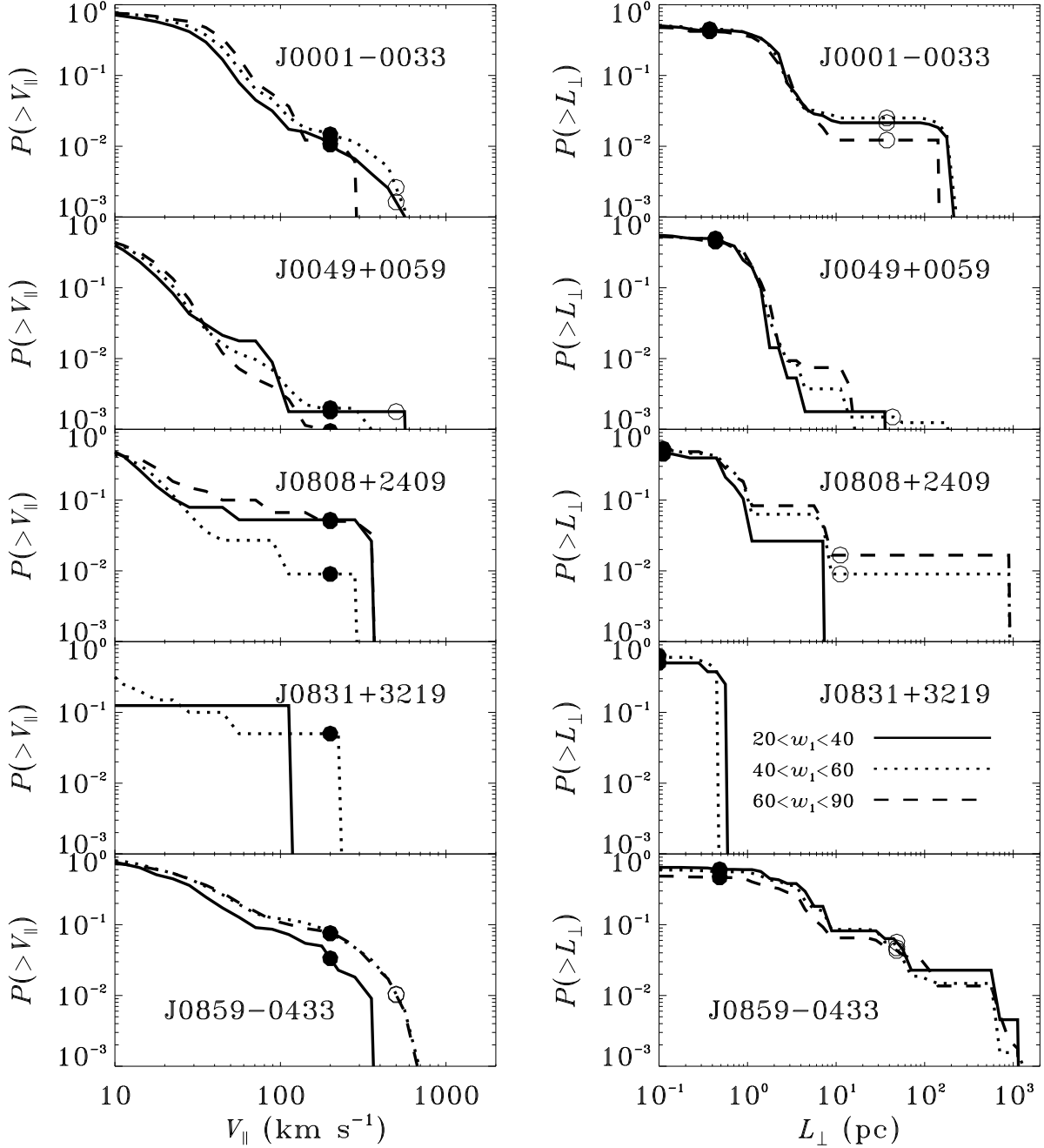


Fig. 6.— Cumulative distribution of LOS velocity V_{\parallel} (Left) and apparent spatial off-center displacements L_{\perp} vertical to LOS (right) for X-shaped radio objects J0001-0033, J0049+0059, 3C192, J0831+3219, and J0859-0433. The dots and circles in the left panels mark, respectively, the locations of $V_{\parallel} = 200$ km s $^{-1}$ and 500 km s $^{-1}$, while those in the right panels mark, respectively, the locations of $\theta_{\perp} = 10$ mas and 0.1 mas.

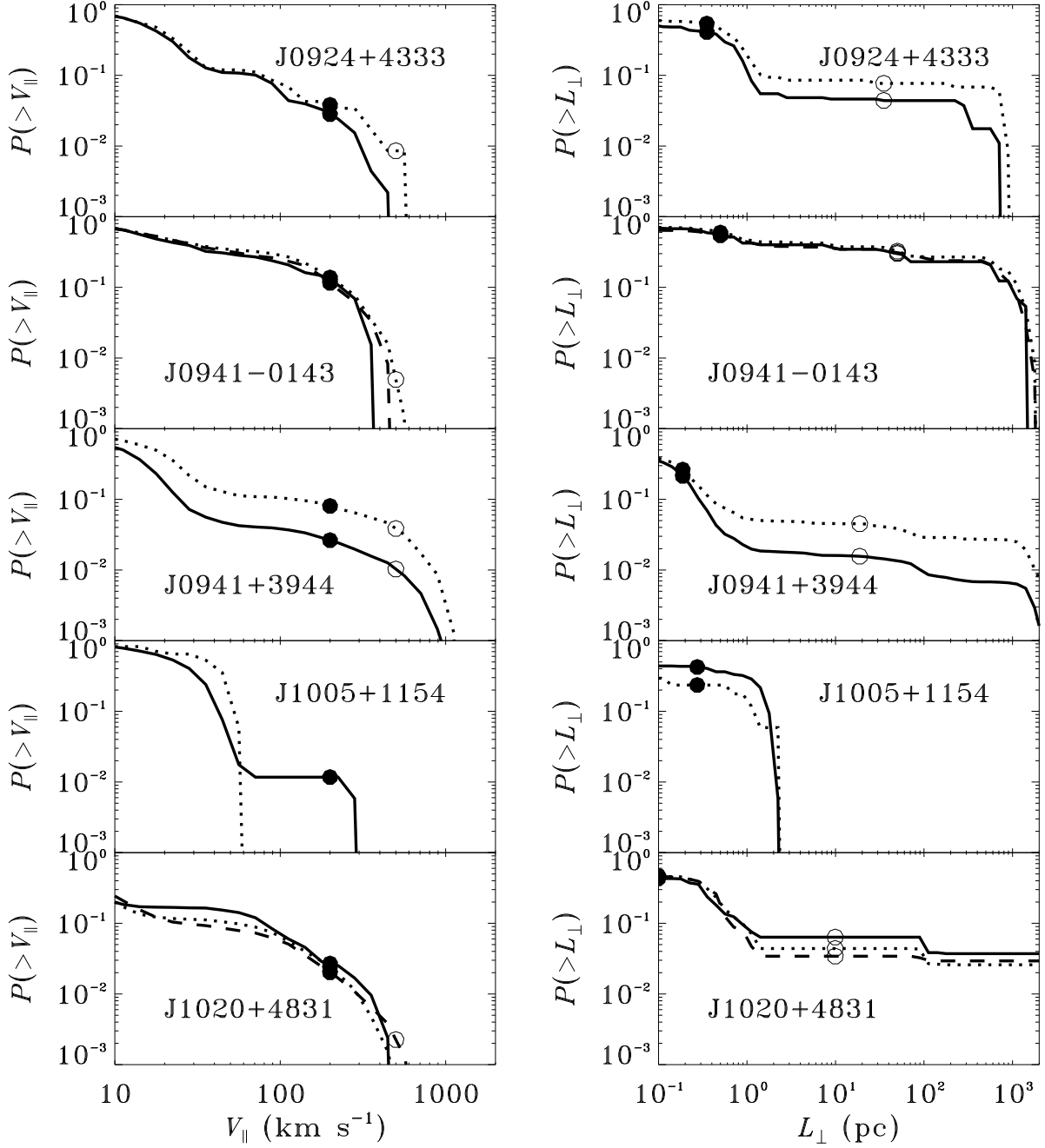


Fig. 7.— The same as Figure 6 but for objects J0924+4333, J0941-0143, 3C223.1, J1005+1154, 4C+48.29.

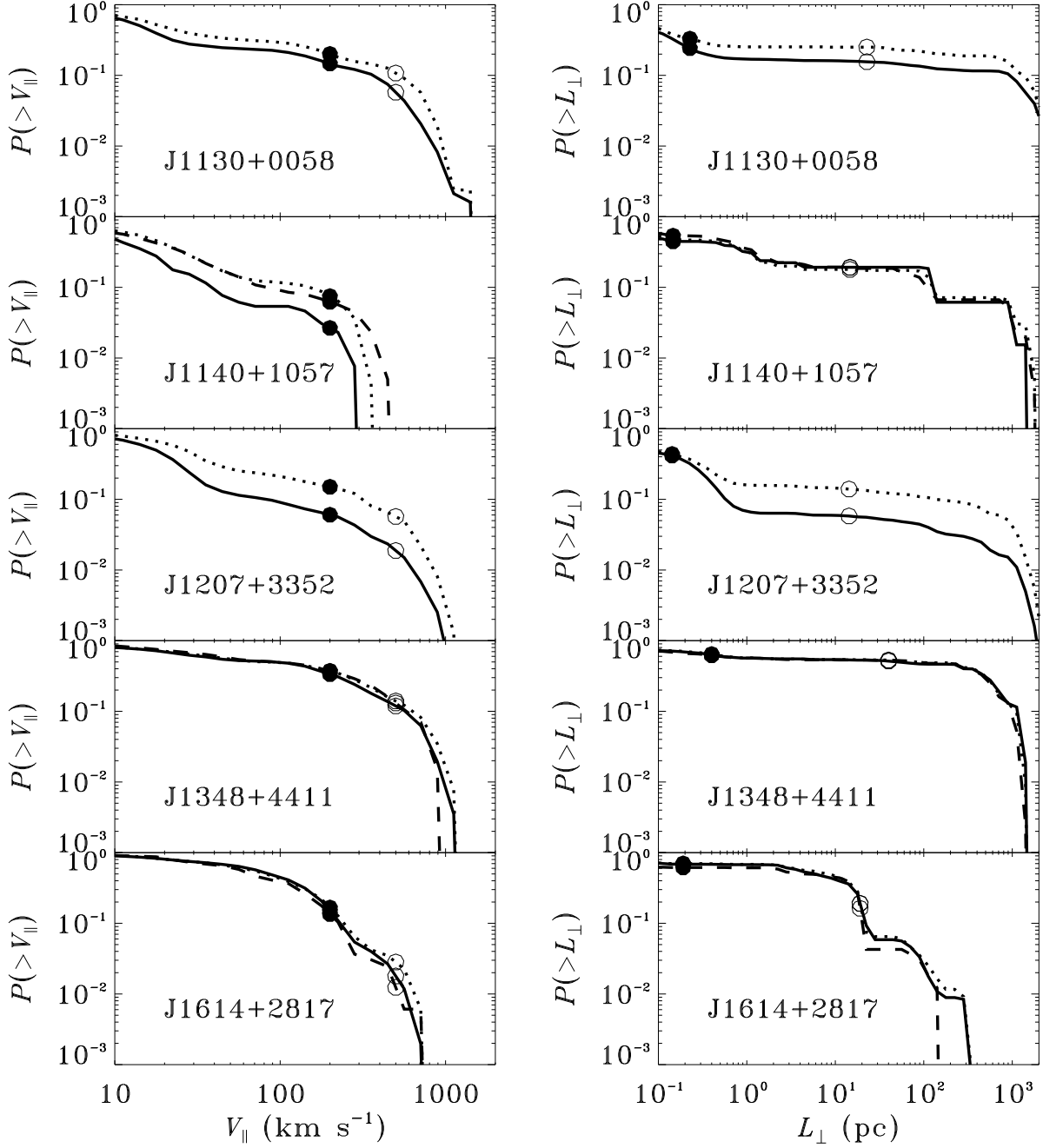


Fig. 8.— The same as Figure 6 but for objects 4C+01.30, J1140+1057, J1207+3352, J1348+4411, and J1614+2817.

Table 1. X-shaped samples

IAU Name	ID z	$\log M$ [M_{\odot}]	$\log \lambda L_{\lambda}(5100\text{\AA})$ [erg s $^{-1}$]	δ [$^{\circ}$]	w_2 [$^{\circ}$]	$\log t_a$ [yr]	ref	V_{cr} [10 2 km s $^{-1}$]	V_{dp} [10 2 km s $^{-1}$]	w_1 [$^{\circ}$]	$P_{v,\parallel}$ [%]	$P_{\theta,\perp}$ [%]	P_{dp} [%]
(1)	(2)	(3)	(4)	(5)	(6)	(7)	(8)	(9)	(10)	(11)	(12)	(13)	(14)
J0001–0033	G 0.247	8.70	43.77	60 ± 7.5	45~70	6.37	1,3,4	34	7.5	20~40 40~60 60~90	0.16, 1.1 0.26, 1.5 0.0, 1.2	2.1, 43 2.5, 45 1.2, 42	50 $^{72}_{13}$ 50 $^{71}_{14}$ 55 $^{76}_{12}$
J0049+0059	G 0.304	8.73	43.43	60 ± 20	60~90	6.68	1,3,4	42	9.5	20~40 40~60 60~90	0.18, 0.19 0.0, 0.20 0.031, 0.10	0.0, 50 0.15, 49 0.015, 45	33 $^{64}_{2.0}$ 34 $^{64}_{1.6}$ 33 $^{64}_{1.7}$
J0808+2409 3C192	G 0.060	8.21	43.85	60 ± 7.5	60~90	6.52	2,3,4	18	4.1	20~40 40~60 60~90	0.0, 5.3 0.0, 0.90 0.0, 5.0	0.0, 45 0.90, 53 1.7, 50	77 $^{89}_{57}$ 80 $^{88}_{56}$ 80 $^{88}_{61}$
J0831+3219 4C+32.25	G 0.051	8.08	43.97	65 ± 7.5	60~90	6.69	2,3,4	15	3.3	20~40 40~60 60~90	0.0, 0.0 0.0, 5.0 — ^a	0.0, 50 0.0, 63 — ^a	87 $^{87}_{76}$ 80 $^{85}_{66}$ — ^a
J0859–0433	G 0.356	8.52	— ^c	60 ± 15	60~90	6.08	1,3,4	— ^c	— ^c	20~40 40~60 60~90	0.0, 3.3 1.0, 7.6 1.0, 7.4	5.7, 60 4.7, 56 4.346	— ^c — ^c — ^c
J0924+4233	G 0.227	8.38	43.58	70 ± 7.5	45~70	6.54	1,3,4	26	5.8	20~40 40~60 60~90	0.0, 2.8 0.85, 3.8 — ^a	4.4, 41 7.7, 54 — ^a	63 $^{79}_{30}$ 64 $^{83}_{33}$ — ^a
J0941–0143	G 0.384	7.68	43.19	55 ± 7.5	60~90	6.14	1,3,4	15	3.3	20~40 40~60 60~90	0.0, 13 0.49, 14 0.0, 12	30, 55 32, 59 30, 55	84 $^{90}_{68}$ 82 $^{91}_{67}$ 82 $^{90}_{67}$
J0941+3944 3C223.1	G 0.107	8.10	43.94	65 ± 7.5	15~35	6.44	2,3,4	15	3.4	20~40 40~60 60~90	1.0, 2.6 3.9, 8.0 — ^a	1.5, 21 4.5, 26 — ^a	75 $^{86}_{54}$ 80 $^{89}_{62}$ — ^a
J1005+1154	G 0.166	8.67	44.12	75 ± 7.5	45~70	6.43	1,3,4	26	6.0	20~40	0.0, 1.1	0.0, 42	58 $^{76}_{25}$

Table 1—Continued

IAU Name	ID z	$\log M$ [M_{\odot}]	$\log \lambda L_{\lambda}(5100\text{\AA})$ [erg s $^{-1}$]	δ [$^{\circ}$]	w_2 [$^{\circ}$]	$\log t_a$ [yr]	ref	V_{cr} [10 2 km s $^{-1}$]	V_{dp} [10 2 km s $^{-1}$]	w_1 [$^{\circ}$]	$P_{v,\parallel}$ [%]	$P_{\theta,\perp}$ [%]	P_{dp} [%]
(1)	(2)	(3)	(4)	(5)	(6)	(7)	(8)	(9)	(10)	(11)	(12)	(13)	(14)
										40~60 60~90	0.0, 0.0 — ^a	0.0, 23 — ^a	51 ⁵⁹ ₃₂ — ^a
J1020+4831 4C+48.29	G 0.053	8.08	43.78	45 \pm 7.5	60~90	6.72	2,3,4	16	3.7	20~40 40~60 60~90	0.0, 2.7 0.050, 2.4 0.22, 2.0	6.3, 43 4.3, 46 3.4, 47	76 ⁸⁵ ₅₉ 77 ⁸⁷ ₅₈ 78 ⁸⁷ ₆₀
J1101+1640	G 0.069	8.30	43.69	72 \pm 7.5	60~90	6.62	2,3,4	22	5.0	20~40 40~60 60~90	— ^a — ^a — ^a	— ^a — ^a — ^a	— ^a — ^a — ^a
J1130+0058 4C+01.30	Q 0.132	7.65	44.10	80 \pm 7.5	15~35	6.24	3,4,5	8.3	1.9	20~40 40~60 60~90	5.8, 15 11, 20 — ^a	16, 24 25, 33 — ^a	89 ⁹⁵ ₈₀ 89 ⁹⁶ ₈₁ — ^a
J1140+1057	G 0.081	8.10	43.61	55 \pm 7.5	60~90	6.28	1,3,4	18	4.1	20~40 40~60 60~90	0.0, 2.7 0.0, 7.5 0.0, 6.2	19, 45 18, 47 19, 54	78 ⁸⁷ ₅₇ 76 ⁸⁷ ₅₇ 76 ⁸⁷ ₅₅
J1207+3352	G 0.079	7.96	44.13	65 \pm 7.5	15~35	6.19	1,3,4	12	2.6	20~40 40~60 60~90	1.9, 6.0 5.7, 15 — ^a	5.8, 41 14, 44 — ^a	82 ⁹¹ ₆₇ 85 ⁹² ₇₄ — ^a
J1210–0341	G 0.178	8.30	43.90	82 \pm 7.5	45~70	5.97	1,3,4	20	4.4	20~40 40~60 60~90	— ^a — ^a — ^a	— ^a — ^a — ^a	— ^a — ^a — ^a
J1327–0203	G 0.183	8.43	44.01	80 \pm 7.5	60~90	6.39	1,3,4	22	4.8	20~40 40~60 60~90	— ^a — ^a — ^a	— ^a — ^a — ^a	— ^a — ^a — ^a
J1348+4411	G 0.267	7.05	43.28	65 \pm 15	45~70	5.87	1,3,4	6.7	1.5	20~40 40~60	12, 33 14, 37	51, 63 53, 64	93 ⁹⁷ ₈₆ 91 ⁹⁶ ₈₅

A. Deceleration of recoiling SMBH due to dynamical friction

We set up an 1-D analytic model to calculate the deceleration of a recoiling SMBH due to dynamical friction against stars and dark matter (DM). We adopted a core-Sérsic law (Terzić & Graham 2005) for the stellar density distribution and an NFW profile for DM halo (Volonteri et al. 2003). The normalization of the density is determined by the conditions that (1) the mass ratio between SMBH and host galaxy is $M_{\bullet}/M_g = 0.002$ and (2) the mass deficit (Merritt 2006) inside core radius equals the mass of SMBH. Interested readers are referred to Gualandris & Merritt (2008) for more detailed discussions on the density distribution of host galaxy.

For a recoiling supermassive black hole with mass M_{\bullet} at galactic centers $r = 0$ obtaining an initial kick velocity $v = v_k$, the N-body numerical simulations (Merritt 2006; Li et al. 2011) suggests that the dynamical evolution of recoiling black hole within the host galaxy and dark halo can be divided into three phases and is well described by the equations incorporating the Chandrasekhar formula for dynamical friction

$$\frac{dr}{dt} = v \quad (\text{A1})$$

$$\frac{dv}{dt} = -\frac{GM_g(r)}{r^2} - 4\pi \ln \Lambda G^2 M_{\bullet} \rho(r) \frac{v}{|v|^3} \left[\text{erf}(X) - \frac{2X}{\sqrt{\pi}} e^{-X^2} \right], \quad (\text{A2})$$

where $M_g(r)$ is the total mass inside the sphere of radius r about the galaxy center, $\ln \Lambda$ is the Coulomb logarithm, $\rho(r)$ is the total density of stars and dark matter, $X = v/\sqrt{2}\sigma(r)$, and $\sigma(r)$ is the stellar velocity dispersion at r . The N-body simulation given by Merritt (2006) shows that when the total mass within the orbit of the oscillating black hole is larger than the black hole mass M_{\bullet} , the dynamic evolution of recoiling black hole is at Phase I and the fiducial Coulomb logarithm is $\ln \Lambda = 2.5$. However, when the stellar mass within the orbit of black hole become smaller than M_{\bullet} , the dynamic evolution of recoiling black hole goes into an long-term oscillatory Phase II during which the Coulomb logarithm is in the range $0.1 \lesssim \ln \Lambda \lesssim 0.3$ with a typical value $\ln \Lambda \simeq 0.2$ (Figure 10 of Gualandris & Merritt 2008). At a much later time of Phase III, the black hole reaches a thermal equilibrium with stars and has a Brownian motion at the galaxy center (Gualandris & Merritt 2008). For the cases which we are interested in, the black hole never goes into Phase III and we will not considered it here.

Figure 9 shows the resulting evolution of r as a function of time t , where r is normalized by the effective radius of the host galaxy, R_e , and t is normalized by the dynamical timescale T_e at R_e . Different trajectories are for different initial kick velocity v_k , which is normalized by the escape velocity v_{esc} of the host galaxy and listed in the legend. Our model is essentially the same as Model A2 in Gualandris & Merritt (2008), except that the ratio M_{\bullet}/M_g in our

Table 1—Continued

IAU Name	ID z	$\log M$ [M_{\odot}]	$\log \lambda L_{\lambda}(5100\text{\AA})$ [erg s $^{-1}$]	δ [$^{\circ}$]	w_2 [$^{\circ}$]	$\log t_a$ [yr]	ref	V_{cr} [10 2 km s $^{-1}$]	V_{dp} [10 2 km s $^{-1}$]	w_1 [$^{\circ}$]	$P_{v,\parallel}$ [%]	$P_{\theta,\perp}$ [%]	P_{dp} [%]
(1)	(2)	(3)	(4)	(5)	(6)	(7)	(8)	(9)	(10)	(11)	(12)	(13)	(14)
										60~90	13, 37	53, 62	94 $^{97}_{88}$
J1444+4147	G 0.188	8.34	43.74	68 ± 7.5	60~90	6.60	1,3,4	23	5.1	20~40 40~60 60~90	— ^a — ^a — ^a	— ^a — ^a — ^a	— ^a — ^a — ^a
J1614+2817	G 0.108	9.08	44.02	60 ± 7.5	45~70	5.59	1,3,4	45	10	20~40 40~60 60~90	1.8, 15 2.8, 17 1.2, 13	19, 69 19, 70 16, 62	29 $^{61}_{0.78}$ 29 $^{60}_{0.92}$ 33 $^{65}_{0.0}$

^athere are no solutions in our Monte Carlo calculations with 10 8 random number experiments

^bThis source belongs to X-shaped quasar

^cno SDSS photometry available

References. — (1) Cheung (2007), (2) Lal & Rao (2007), (3) Landt et al. (2010), (4) Mezcua et al. (2011), (5) Wang et al. (2003)

model is two times greater, which results in a slightly longer dynamical friction timescale than that in Gualandris & Merritt (2008).

Notice that in our simple analytic model, the *normalized* trajectories of $r/R_e(t/T_e)$ and $v/v_{\text{esc}}(t/T_e)$ are uniquely determined by v_k/v_{esc} and do not depend on M_\bullet . This characteristic allows us to derive the trajectories of $r(t)$ and $v(t)$ for any kick velocity v_k and black hole mass M_\bullet , by interpolating among a limited number of *normalized* trajectories pre-calculated for different v_k/v_{esc} values. The normalized trajectories that we used in our Monte Carlo simulations are for $v_k/v_{\text{esc}} = 0.01, 0.05, 0.1, 0.2, 0.3, \dots, 2.0$.

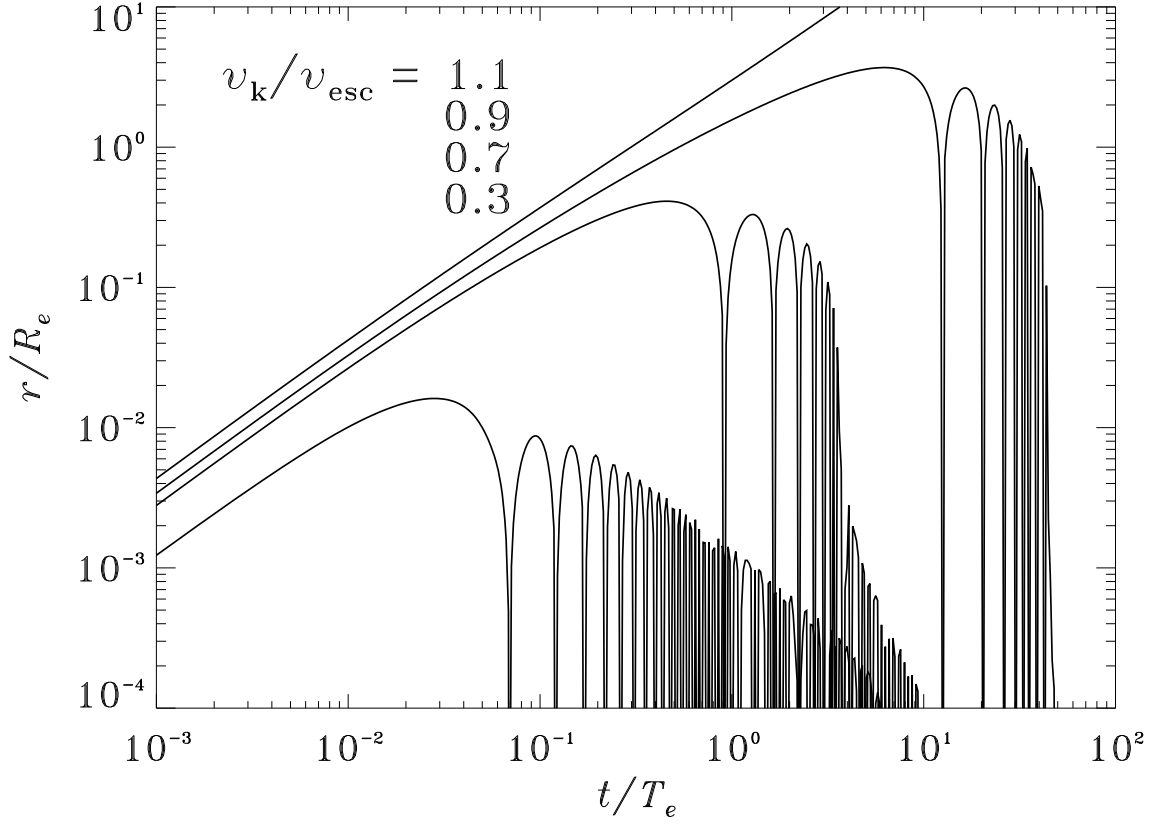


Fig. 9.— Trajectories of recoiling SMBH with different initial kick velocity. Because of the logarithmic scale, the oscillatory phase II (Gualandris & Merritt 2008) is clearly resolved in the plot when $v_k/v_{\text{esc}} = 0.3$ and 0.7.